Monitoring geothermal reservoir developments with the Controlled-Source Electro-Magnetic method - A calibration study on the Reykjanes geothermal field

Mathieu Darnet, Pierre Wawrzyniak, Nicolas Coppo, S. Nielsson, E. Schill, G.Ó. Fridleifsson

Version of Record: https://www.sciencedirect.com/science/article/pii/S0377027317306364
Manuscript_2f0399151c6d1dd608d8a3069c599947

Monitoring geothermal reservoir developments with the Controlled-Source Electro-Magnetic method – A calibration study on the Reykjanes geothermal field

M. Darnet[1], *P. Wawrzyniak*[1], *N. Coppo*[1], *S. Nielsson*[2], *E. Schill*[3], *G.Ó.Fridleifsson*[4]

[1] *BRGM, 3Av.ClaudeGuillemin, 45060Orléans, France*

[2] *Islenskarorkurannsoknir/IcelandGeoSurvey, Grensasvegur9, 108Reykjavik, Iceland*

[3] *KIT, InstitutfurNuklearеEntsorgung, Hermann − von − Helmholtz − Platz1, 76344Eggenstein − Leopoldshafen, Germany*

[4] *HSOrka, Svartsengi, 240Grindavík, Iceland*

Abstract

Surface geophysical monitoring techniques are important tools for geothermal reservoir management as they provide unique information on the reservoir development away from boreholes. For magmatic environments, electromagnetic (EM) methods are attractive monitoring tools as they allow to characterize the reservoir and hence potentially monitor changes related to fluid injection/production. Indeed, the electrical resistivity of reservoir rocks is highly dependent on the volume, chemistry and phase of the in-situ geothermal brine (e.g. liquid, vapor, supercritical).

Passive EM techniques (e.g. magnetotellurics or MT) are traditionally used for geothermal exploration and a few recent studies have demonstrated its potential for monitoring reservoir development. One of the main challenges is though the presence of cultural noise and/or variability of the Earth magnetic field that can obfuscate the EM signals of interest. We have investigated the benefits and drawbacks of active EM surveying (Controlled-Source EM or CSEM) to tackle this challenge, first with a synthetic study and subsequently with an actual time-lapse survey acquired in 2016 and 2017 over the Reykjanes geothermal field in Iceland before (baseline) and after (monitor) the thermal stimulation of the supercritical RN-15/IDDP-2 geothermal well.

The synthetic study showed that for geothermal fields having a resistivity structure similar to the Reykjanes field (i.e. a conductive caprock overlying a more resistive higher temperature reservoir), CSEM and MT measurements can detect resistivity changes within the deep resistive reservoir, provided that measurement errors are small. Variations in many survey parameters (e.g. errors in receiver position/orientation, differences in recording devices, variations of near surface conditions, external noise) can create significant time-lapse CSEM measurement errors. Our actual time-lapse survey showed that when similar CSEM equipment is used during the baseline and monitor surveys and systematically d-GPS positioned, the remaining key parameter controlling the survey repeatability is the level of

external noise. Since the influence of external noise on CSEM data can be artificially reduced (e.g. by increasing the transmitter dipolar moment), it offers the possibility to adapt the survey design to increase the chance of detecting the time-lapse signals of interest. On the contrary, little control is possible on the MT signal to noise ratio and hence repeatability.

The time-lapse EM survey acquired over the Reykjanes geothermal reservoir showed indeed that a high CSEM survey repeatability can be achieved with electric field measurements (within a few percent) but that time-lapse MT survey is a challenging task because of the high level of cultural noise in this industrialized environment. To assess the quality of our CSEM dataset, we inverted the data and confronted the resulting resistivity model with the resistivity logged in the RN-15/IDDP-2 well. We obtained a good match up to 2-3km depth, i.e. enough to image the caprock and the liquid-dominated reservoir but not deep enough to image the reservoir in supercritical conditions. To obtain such an image, we had to jointly invert legacy MT data with our CSEM data. On the monitoring aspects, the analysis of changes in electric fields did not allow to identify any CSEM signal related to the thermal stimulation of the RN-15/IDDP-2 well. One possible explanation is the weakness of the time-lapse CSEM signal compared the achieved CSEM survey repeatability as a result of a limited resistivity change over a limited volume within the reservoir. Future reservoir developments in the supercritical reservoir (e.g. hydraulic stimulation, long-term fluid circulation) will most likely generate stronger resistivity variations over a larger volume than during the thermal stimulation of the well. This calibration study provides the basic information for deciding when and how an EM monitor survey must be performed for the monitoring of the Reykjanes geothermal reservoir but also for the definition of the monitoring strategy of similar high-enthalpy geothermal reservoirs.

Keywords: Controlled-Source Electro-Magnetic, Magneto-Telluric, monitoring, time-lapse, geothermal reservoir, MT, CSEM

1. Introduction

The DEEPEGS project is exploring the technical and economic feasibility of producing supercritical geothermal resources. The RN-15/IDDP-2 well is located in the Reykjanes saline geothermal system in South-West Iceland, on the landward extension of the Mid-Atlantic Ridge. The drilling of the wellbore RN-15/IDDP-2 began in August 2016 and the well was completed at a depth of 4659 m MD (Measured Depth, 4.5 km vertical depth) in January 2017. Supercritical conditions were encountered at the bottom (measured temperature: 426°C , but estimated around 500-530°C, 340 bar pressure; Frileifsson et al. (2017), Stefanson et al. (2017)). Stimulations in the form of cold-water injection (mainly thermal stimulations) have been performed to connect the wellbore to existing hydraulic pathways, i.e. pre-existing natural fracture network, in order to improve the productivity of the well

Email addresses: m.darnet@brgm.fr
(M. Darnet[1]), p.wawrzyniak@brgm.fr(*P. Wawrzyniak*[1]), n.coppo@brgm.fr(*N. Coppo*[1]), Steinthor.Nielsson@isor.is(*S. N*

and hence increase the chance of harnessing the energy contained in the super-critical fluid (Reinsch et al. (2017)). The implementation of geophysical field monitoring methods was required to characterize the impact of such stimulation on its environment, in particular 1) prior to the operation to obtain a reference state unrelated to the field development and 2) during and after the stimulation operation to evaluate its impact on the geothermal reservoir development.

Among the geophysical methods applicable on high enthalpy geothermal systems, the electromagnetic (EM) methods are of prime importance as they offer the unique opportunity to characterize some of the key ingredients of an economically exploitable geothermal system, like the presence of geothermal fluids, the geometry of the permeable reservoir and associated impermeable clay cap and its temperature (Spichak and Manzella (2009), Munoz (2014)). Indeed, the lower temperature (<230 °C) smectite clay alteration products are more electrically conductive than their higher temperature (>230 °C) chlorite-epidote clay counterparts due to loosely bound cations in smectite (Leroy and Revil (2004); Munoz (2014); Kristinsdóttir et al. (2010)). In addition, the presence of in-situ geothermal brine in the pore space usually lowers significantly the electrical resistivity of the medium (Archie et al. (1942)). Similarly, the increase of temperature generally lowers the rock electrical resistivity, through an increase of the fluid and surface conductivity (Kristinsdóttir et al. (2010)). At higher temperatures and above the brine critical point, the combination of lower viscosity reduction, thermal expansion and decrease of the dielectric constant results in a sharp decrease in the brine conductivity (Kummerow and Raab (2015)). Laboratory experiments on synthetic Reykjanes geothermal brine showed that its conductivity indeed decrease by a factor 5 to 7 when crossing the critical point around 405 °C (Reinsch (2016)). For geothermal systems like Reykjanes, it is therefore expected that the rock resistivity strongly varies with depth with a shallow conductive clay cap (smectite rich, temperature <230°C) overlying a more resistive high temperature medium (chlorite/epidote rich, temperature >230°C), subsequently possibly even more resistive when crossing the critical point (chorite/epidote rich material with supercritical fluid, temperature >405°C). Such a sensitivity of the rock electrical resistivity makes it a parameter of choice to characterize the reservoir geometry and hence potentially monitor changes related to fluid injection/production.

Electromagnetic monitoring is becoming increasingly popular, including magnetotelluric (MT) monitoring of hydraulic stimulation of enhanced geothermal reservoirs (Peacock et al. (2013); Didana et al. (2017), Thiel (2017),Abdelfettah et al. (2018)), MT monitoring of hydraulic fracturing of tight hydrocarbon reservoirs (Orange et al. (2009); Rees et al. (2016a,c,b)), DC resistivity and Controlled-Source Electromagnetic (CSEM) monitoring of CO_2-sequestration scenarios (Streich et al. (2010); Börner et al. (2015b,a); Streich (2016)), and CSEM monitoring of heavy oil recovery using a borehole–surface configuration (Tietze et al. (2015)). One of the main challenges of passive EM monitoring (MT) remains the variability of the Earth magnetic field variations that may lead to poor signal to noise data and hence unreliable MT recordings at the times of interest (Abdelfettah et al. (2018)). In addition, industrial activities can sometimes generate low frequency EM noise that can obfuscate the MT signals of interest (Streich et al. (2013)).

To increase the signal to noise and hence reliability of EM monitoring techniques, we

propose to complement passive MT monitoring experiments with active CSEM surveys to compensate for the occasional weakness of MT signal in specific frequency bands (e.g. dead band) and/or the presence of strong cultural noise. Indeed, active surveying allows to control and hence potentially increase the signal to noise ratio of acquired data at any point in time (e.g. by increasing the transmitter strength and/or increasing the recording times). In addition, the CSEM source configuration can be such that it provides additional information on the resistivity structure at depth that MT data cannot necessarily resolve. For instance, a horizontal electric dipole is often used for direct targeting of thin resistive layers, due to its superior sensitivity to resistors compared to MT (Constable and Weiss (2006); Weidelt (2007); Constable et al. (2009); Commer and Newman (2009)). To test and validate this approach in actual field conditions, we undertook to design and acquire a time-lapse MT and CSEM survey over the Reykjanes geothermal field to assess its ability to characterize and monitor the thermal stimulation of the DEEPEGS/IDDP-2 supercritical reservoir, and more generally, any types of natural and/or forced fluid circulations in geothermal systems (e.g. hydraulic, thermal, acid stimulations; geothermal fluid production; produced fluid reinjection). In this paper, after briefly describing the Reykjanes geothermal field, we will first discuss with a synthetic study the benefits of acquiring CSEM data in addition to MT data for resistivity mapping and monitoring. We will then describe how we have designed, acquired, processed and inverted the time-lapse CSEM/MT surveys in order to obtain a reliable and highly-repeatable EM dataset on this reservoir. We will then conclude with an attempt to identify time-lapse resistivity changes and discuss the remaining challenges towards reliable resistivity monitoring of such high-enthalpy geothermal reservoir development.

2. Reykjanes Geothermal Field

The Reykjanes geothermal system is located at the tip of the Reykjanes peninsula, SW-Iceland (figure 1) at the landward extension of the Reykjanes Ridge. The heat source of the Reykjanes geothermal field is not known but interpreted to be dykes, thin sills or/and a sheeted dyke complex. A brittle-ductile transition is estimated at 5,5-6 km depth which marks the bottom of potential permeability and therefore the base of the hydrothermal system (Gudnason and Flovenz (2015)). Based on geothermal manifestations on surface the aerial extent of the Reykjanes geothermal field is estimated to be 1-1,5 km^2 (Björnsson et al. (1970)) on surface but with greater lateral extent at depths based on resistivity surveys (Karlsdottir and Vilhjalmsson (2014)). The reservoir fluid is of seawater origin but affected by boiling and fluid/rock interaction (e.g. Tómasson and Kristmannsdóttir (1972), Arnórsson (1995), Óskarsson et al. (2015)). Before the production started from the Reykjanes field in 2006 the geothermal reservoir was liquid dominated. Production has caused a pressure draw-down in the centre of the field and therefore a steam cap has formed above 1000-1100 m depth in the reservoir (Gudmundsdottir (2015)).

The reservoir has been in operation for power production since May 2006, when the Reykjanes power plant started generation of 100 MWe with two 50 MWe steam turbines. Installed power capacity is 175 MWe from the two geothermal power plants at Svartsengi,

75 MW, and Reykjaens, 100 MW. In addition, 150 MW thermal energy is generated for district heating and supplies fresh water to the municipalities at the Reykjanes peninsula. Average production from the reservoir at about 2km depth is 500 kg/s of 220°C geothermal fluid at 22 bar Well Head Pressure.

3. CSEM and MT sensitivity study

3.1. Reykjanes conceptual resistivity model

In order to study the sensitivity of the CSEM and MT methods for the characterization and monitoring of high-enthalpy geothermal reservoir, we have first designed a simplified 1D resistivity model of the Reykjanes reservoir based on the existing conceptual geological models (Flóvenz et al. (1985), Kristinsdóttir et al. (2010), Khodayar et al. (2016)), resistivity logs (figure 2) and MT soundings (Karlsdóttir and Vilhjálmsson (2016)). It consists in a relatively unaltered and hence resistive (100 Ωm) layer overlying a more conductive (1 Ωm) smectite-zeolite rich zone (figure 3); then, follows a more resistive (30 Ωm) chlorite-epidote rich zone until supercritical conditions are met (at 4km depth in RN-15/IDDP-2 well). At this point, only a handful of studies have measured in laboratory conditions the behavior of the rock electrical resistivity but it is likely that it increases due to the drop of the brine electrical conductivity (Reinsch (2016),Nono et al. (2018)). A factor three increase of the resistivity on different Icelandic rock samples has been observed (Reinsch (2016)), most likely caused by the combination of lower viscosity reduction, thermal expansion and decrease of the dielectric constant (Kummerow and Raab (2015),Nono et al. (2018)). We therefore assumed that the chlorite-epidote rich zone in supercritical conditions is three times more resistive than the chlorite-epidote rich zone (i.e. 100 Ωm). Depths of the different interfaces have been defined based on the existing conceptual geological models of the Reykjanes geothermal field and well data. To study the sensitivity of the CSEM and MT methods to resistivity changes at the reservoir depth, we assumed that its resistivity drops by a factor three over a 1km thick section at 4km depth, simulating a change of geothermal fluid from supercritical to liquid due thermal cooling, as expected during the thermal stimulation of the RN-15/IDDP-2 well.

3.2. MT sensitivity study

We have first computed the MT impedance tensor on the aforementioned 1D resistivity models and subsequently calculated the detectability D of a time-lapse MT signal between two surveys A and B as (Ogaya et al. (2016), Thiel (2017)):

$$D^{\rho}_{MT} = |\rho_B - \rho_A| / \sqrt{\epsilon_A^2 + \epsilon_B^2} \tag{1}$$

where ρ is the MT apparent resistivity (Ωm) and ϵ is the measurement error (Ωm). Frequencies are logarithmically distributed from 0.001Hz until 100Hz. Figure 4 displays the apparent resistivity curves for the simplified 1D resistivity model of the Reykjanes geothermal field (figure 3) as well as the detectability D of the signal caused by the 100Ωm to 30Ωm resistivity drop at 4km depth. Here, we assumed a 1% measurement error on the

apparent resistivities on the base and monitor surveys (Ogaya et al. (2016)). Detectability is maximum at low frequencies (< 0.1Hz) and tops around 5.

3.3. CSEM sensitivity study

Similarly to the MT case, we have first computed the CSEM impedance tensor on the aforementioned 1D resistivity models based on the CSAMT formulation (Zonge et al. (1991)) and subsequently calculated the detectability D of a time-lapse CSEM signal between two surveys A and B as:

$$D^{\rho}_{CSEM} = |\rho_B - \rho_A| / \sqrt{\epsilon_A^2 + \epsilon_B^2} \tag{2}$$

where ρ is the CSEM apparent resistivity (Ωm) and ϵ is the measurement error (Ωm). CSEM fundamental frequencies range from 1/32s until 32Hz and increase by a factor 4, as typically used during CSEM field surveys (Coppo et al. (2016)). We also calculated the CSEM response for the first fourth odd harmonics of the aforementionned fundamental frequencies to obtain a well sampled spectrum from 1/32s until 100Hz. Figure 4 displays the CSEM apparent resistivity curves for the simplified 1D resistivity model of the Reykjanes geothermal field (figure 3) as well as the CSEM detectability D of the signal caused by the 100Ωm to 30Ωm resistivity drop at 4km depth. Here also, we assumed a 1% error on apparent resistivities as observed on our actual measurments (see next section). Detectability is high at low frequencies (< 1Hz) and long transmitter-receiver offset (10km). Detectability tops around 10 at intermediate frequencies (0.1 - 1Hz) i.e. in the transition zone between the far and near-field CSEM response (Zonge et al. (1991)).

3.4. MT vs CSEM sensitivity

The CSEM and MT detectability computed on the simplified 1D resistivity model of the Rekjanes geothermal field (figure 4) shows that for a similar noise level over the whole frequency band, the sensitivity to a resistivity change within the resistive reservoir is likely to be higher on CSEM data than on MT data, most likely due to the superior sensitivity of the CSEM technique to resistors compared to MT (Constable and Weiss (2006); Weidelt (2007); Constable et al. (2009); Commer and Newman (2009)). In addition, the use of a CSEM transmitter allows to control and hence potentially decrease the measurement error on apparent resistivities. This provides an unique opportunity to increase the detectability and hence sensitivity of the EM monitoring method to resistivity changes at the reservoir level (Siripunvaraporn et al. (2018)).

4. Reykjanes time-lapse EM surveys

4.1. Survey design

A pre-survey modelling study was performed to define the best CSEM transmitter configuration as well as the appropriate set of frequencies. An a-priori 2.5D resistivity model (i.e. 3D model with one axis of symmetry) was designed based on the aforementioned conceptual 1D resistivity model of the Reykjanes geothermal reservoir (figure 4). Here also,

we made the assumption that the injection of cold water during the thermal stimulation of the RN-15/IDDP-2 well is lowering the resistivity of the stimulated zone and hence it is getting three times more conductive than the initial state (dropping from 100 Ωm to 30 Ωm). It is challenging to predict the size of the stimulated zone but for simplicity and as a reference case, we assumed that a 1km thick supercritical reservoir section is affected and that it extends laterally over 3km (figure 4).

We subsequently modelled the CSEM response of this model using the MARE2DEM finite-element code developed by Key and Ovall (2011). To do so, we assumed that a horizontal electric dipole transmits a CSEM signal at different frequencies (from 1/32s until 2Hz) into a grid of 500m-spaced receivers. Since CSEM impedance are not directly measured in the field, we focused on electric and magnetic field measurements. Furthermore, we looked into electric field measurements rather the magnetic fields due to their higher sensitivity to resistive anomalies when transmitted by a horizontal electric dipole (Grayver et al. (2014)). We first computed the amplitudes of the major axis of the polarization ellipse (PE) of the horizontal electric field as function of the CSEM frequency and position of the receivers, before and after the stimulation, and subsequently derived the detectability of the time-lapse CSEM signal using equation 2, where the amplitudes of the electric field is used instead of apparent resistivities (figure 5). We assumed that measurement errors range from 0.1% to 10% of the total electric field, as typically observed in actual surveys (see next section). The time-lapse signal is maximal at long transmitter-receiver offsets (>5000m) and low frequencies (<2Hz). Also, the longer the offset, the stronger the anomaly is. Detectable time-lapse signals (i.e. D much greater than 1) require measurement errors in the 1% range or less, highlighting the need for very high repeatability time-lapse CSEM surveys in order to be able to sense such a change. As a consequence, we designed the time-lapse CSEM surveys over the Reykjanes reservoir such that long-offset (>5km) and low-frequency (<2Hz) signals could be measured with a high degree of repeatability. This posed a real challenge due to logistical constrains on the narrow Reykjanes peninsula and expected high-level of EM noise related to the presence of the geothermal plants.

4.2. Time-lapse EM data acquisition

Time-lapse CSEM surveys have been acquired in September 2016, while drilling of RN-15/IDDP-2 well and in August 2017, after the thermal stimulation of the well. It used a double orthogonal horizontal electric dipole for the transmitter (figure 1), 3km north of the geothermal field providing two polarizations called POL1 (900m-long dipole between E1 and E2) and POL2 (900m-long dipole between E2 and E3). Its position is such that the mid-point of the longest transmitter-receiver offsets (7km) is located in the vicinity of the target of interest and such that injection electrodes can be installed in conductive superficial material (here, a swamp) to ensure a good electrical coupling of the transmitter with the ground. In the end, we managed to inject repeatably a current of about 30A at 560V with a Metronix TXM22 during both baseline and monitor CSEM surveys. This signal was successfully picked up by all our CSEM stations deployed over the Reykjanes peninsula (figure 1). To adequately characterize the subsurface, a broad band set of CSEM frequencies (from 1/32s up to 1024Hz) was acquired with a minimum set of 50 cycles at low-frequencies to ensure

proper stacking of any random noise. The waveforms were seven square waves of fundamental frequencies ranging from 1/32s up to 128Hz increasing with a factor 4. A total number of 22 CSEM recording stations were deployed during the baseline and monitor surveys. They were Metronix ADU07 acquisition systems, MFS07 or MFS06 magnetic coils and two orthogonal 100m long electric dipoles oriented North-South and East-West. MT data have been acquired with the same equipment during the night shifts of the baseline survey i.e. when the CSEM transmitter was off. Given the results of the baseline MT survey (see section MT analysis), MT stations were only deployed a couple of hours during the monitor survey, not long enough on the ground to provide reliable low-frequency MT data. Finally, Transient EM (TEM) soundings using a 50m-wide square loop acting as a transmitter and receiver and transmitting an alternating on/off 4A current have been acquired to characterize the near surface resistivity (<200m) and to perform static shift corrections, if necessary (see next section). All recording equipment (electrodes, magnetometers, recording units) have been positioned with a differential GPS with a centimeter accuracy and replaced at the same position during the monitor survey to minimize positioning errors. When possible, electrodes and magnetometers have been put back in the same holes into the ground. Similarly, the transmitter electrodes and cables have been dGPS positioned and re-installed at the same position during the monitor survey.

4.3. MT analysis

4.3.1. MT data processing

The Magnetotelluric method studies the transfer function (hereafter TF), in frequency domain, between the natural electric E and the magnetic field H, recorded at ground surface (Cagniard (1953), Vozoff (1972)), also called the *impedance tensor* Z. The MT impedance contains information about the geo-electric structure for the subsurface. The MT theory is based on the hypothesis of plane wave sources and stationarity of the signals.

Assuming one station location, a fixed frequency f, a $\mathbf{e_i}$ N vector (N corresponds to the number of Fourier coefficients obtained from successive and overlapping subdivision of time series) of horizontal electric field Fourier transform along direction i and a $2xN$ vector of magnetic field $\mathbf{b}$ (two horizontal directions), both quantities are linked by the following equation

$$\mathbf{e_i} = \mathbf{b} \cdot \mathbf{z_i} + \epsilon \tag{3}$$

where $\mathbf{z_i}$ is the magnetotelluric impedance associated with the direction i of the electric field (vector of dimension 2, $z_i = [z_{ix} z_{iy}]$) and ϵ is the a vector of random errors.

Equation 3 can be solved using ordinary least-square estimates (Sims et al. (1971)), but often furnishes biased estimates due to local correlated noise between e and h. To overcome this bias, the remote reference method, (hereafter RR) consists in introducing magnetic field data from one (Goubau et al. (1978)) or several (Chave and Thomson (2004)) distant MT station in order to filter noise impact in the least square estimate, provided the RR site and the local station are not contaminated by correlated noise.

Chave and Thomson (2004) introduced the two-stage implementation of the remote reference method . Considering a set of q remote reference horizontal magnetic field reunited in one vector $\mathbf{Q}$ (size $px2$), the local magnetic field is linked to $\mathbf{Q}$ by

$$\mathbf{b} = \mathbf{Q} \cdot \mathbf{W} + \epsilon \tag{4}$$

where $\mathbf{W}$ is a TF between local and remote magnetic field sites. The predicted local magnetic field $\hat{\mathbf{b}}$ is given by

$$\hat{\mathbf{b}} = \mathbf{Q} \cdot \hat{\mathbf{W}} \tag{5}$$

The two-stage RR method consists in replacing $\mathbf{b}$ in equation 3 by $\hat{\mathbf{b}}$ and solve the system.

Unfortunately, due to non-stationarity of the MT signals and transient noise to signal fluctuations, the simple least-square solution leads to unreliable estimates. In order to overcome those problems, robust methods were introduced in the 80's. Two principal robust methods are commonly used to estimate the MT transfer function (Chave and Jones (2012)).

The first is the M-estimator is a robust TF estimator , designed to minimize the influence of data associated to large electric field residuals in the regression (Chave and Thomson (1989)). M-estimator TFs provides a good protection against strong data residuals but are still highly sensitive to extreme values in the magnetic field (predictor), *i.e.* the so called *leverage points*. The second method is the bounded influence estimator (Chave and Thomson (2004)), which consists in a variation of the M-estimator where the diagonal weighting matrix is enhanced to provide protection against leverage points. In this paper, we use the Razorback Python library (Smai and Wawrzyniak (submitted)) to perform two-stage multiple remote reference bounded influence processing.

4.3.2. MT results

Seven stations were used for MT acquisition during the baseline survey (see figure 1). Each MT station dataset consists in one hour of recordings at 4096Hz sampling frequency and at least 12 hours at 512 Hz. A distant synchronous MT station, located 80 km away, was used as a remote reference (hereafter site 100).

MT sounding consistency quality assessment was performed using apparent resistivity and phase curves inter-comparison between single site and combinations of remote reference results. Phase tensor consistency analysis was performed, as advocated by Booker (2014): " Smooth variation of the phase tensor with period and position is a strong indicator of data consistency.".

In order to asses the quality of the MT data in the [1 mHz-128 Hz] band, we show the normalized phase tensor (hereafter PT), i.e the phase tensor with longer axis Φ_{max} normalized to 1, is displayed for all frequency and RR combination. Ellipses are filled with a color bar indexed either on their their ellipticity value (left panel on figure 6) or their β angle (right panel, same figures). Low values of ellipticity diagnose à 1D medium (Bibby et al. (2005) while β angles absolute values below 3° diagnoses a 2D medium (Booker (2014)).

In any remote reference combination (indexed by vertical scale ticks on figure 6), discontinuous PT behavior are observed for 4 soundings (sites 9 10 11 and 24), leading to rejection of those data for interpretation. Site 13 display a smoother and coherent behavior in the high frequency (above 1 Hz) when combined with sites 10 and 100. Site 15 display smooth PT behavior at frequencies below 0.1 Hz and above 5 Hz.

"Best" soundings 00, 13 and 15 are displayed on figure 7 for single site (SS) processing and maximum number of RR two-stage processing. Error bars on both phase and apparent resistivity are significantly larger on multiple RR curves. Consistently with figure 6, MT soundings are inconsistent in the [0.1-5] Hz frequency band for site 15, and below 1 Hz for site 13. SS curves shows non physical apparent resistivity decreases (up to 3 order of magnitude decrease on ρ_{yx} for site 13) in the [0.05-5] Hz band, which tends to disappear on the RR curves. Still RR curves are scattered. On site 00, MT curves are smoother in SS mode.

Due to intense anthropogenic activity in the area during RN-15/IDDP-2 drilling phase, MT soundings are of bad quality and cannot be used for interpretation. Despite the use of combinations between local and distant remote reference and bounded influence processing, a signal incoming from a near-field source persists in the data and creates either fake resistivity variations or large amplitude scatter in the frequency curves. MT imaging and subsequently monitoring with such EM noise conditions will not lead to reliable enough results. Since the baseline MT were of poor quality, we did not deem necessary to acquire MT data during the monitor time-lapse survey.

4.4. CSEM data processing

Considering a transmitter injecting a square-wave electric current at a frequency f_0 and a set of synchronous EM receivers recording the horizontal components of the electromagnetic field, CSEM data processing consist in estimating frequency domain transfer functions between the receiver's 4 components of the horizontal electromagnetic field (Ex, Ey, Hx Hy) and the transmitter injected current I along each chosen direction of injection.

$$\begin{pmatrix} E_x \\ E_y \\ H_x \\ H_y \end{pmatrix} = \begin{pmatrix} T_{E_x} \\ T_{E_y} \\ T_{H_x} \\ T_{H_y} \end{pmatrix} I \tag{6}$$

TF estimation is performed on the harmonics of the injected frequency f_0. The CSEM TF estimation problem (equation 6) is simpler than the MT one as i) it reduces to TF estimation between one input I and one output (any component of the EM field) and ii) the input I is stationary (no leverage points are expected).

In practice, we estimated CSEM TFs using both simple least-square (hereafter LS) and M-estimator (hereafter ME) techniques, as advocated by Streich et al. (2013), using the RAZORBACK library (Smai and Wawrzyniak (submitted)). In our case, both LS and ME converges to similar results and therefore LS results have been used.

In addition, an estimation of the ambient noise is performed around each frequency $f0$. It is computed as the quadratic mean of all Fourier Transform coefficients contained in the

interval $[f0 - 0.1f0 : f0[U]f0 : f0 + 0.1f0]$ and is considered an estimate of the noise to signal ratio.

4.5. MT and CSEM static shift corrections

Shallow lateral changes of resistivity and topographic features can created charge accumulations at the surface of these inhomogeneities and shift electric field measurements up or down by a factor independent of frequency but phase remains unaffected (Zonge et al. (1991)). To correct for such effects on CSEM and MT data, we shifted the MT apparent resistivity and CSEM amplitude curves by a factor such that high frequency data (> 100 Hz) match the response from a 1D resistivity model built from the 1D inversion of the co-located TDEM sounding. In the end, only the few CSEM/MT stations located close to the geothermal alteration zone outcropping at surface required such corrections.

5. Reykjanes time-lapse CSEM survey repeatability

In this section, we aim at establishing the accuracy at which time-lapse CSEM measurements can be repeated over a period time of several months and what the key parameters that influence it. We focused our attention on the electric field measurements rather the magnetic fields due to their higher sensitivity to resistive anomalies when transmitted by a horizontal electric dipole (Grayver et al. (2014)).

5.1. Influence of CSEM recording equipment and transmitter

To assess the influence of the transmitter and recording equipment on the CSEM survey repeatability, we have performed a CSEM experiment where a 1Hz square is transmitted continuously with a 200m-long horizontal electric dipole and recorded with a set of four ADU07 acquisition systems measuring the horizontal electric field at the same location i.e. all electrodes buried in the same pit. Transmitting and recording electric dipoles are separated by 500m and an in inline configuration (parallel dipoles). We then uninstalled and re-installed a few hours later the electrodes at the same location and compared the repeatability of the electric field measurements. To compensate for the variability of the injected current at the transmitter due to changes of the electrical coupling of the injection electrodes with time (i.e. caused by heating of the ground), the electric fields have been normalized by the injected current measured at the transmitter. We then define the repeatability R of electric field measurements as:

$$R_{AB}{}^{E} = |E_B - E_A|/((E_A + E_B)/2) \tag{7}$$

Where E is the amplitude of the electric field normalized by the transmitter dipolar moment (V/Am^2), A and B refers to the baseline and monitor surveys, respectively. All measurements fall within a 0.1% repeatability range, demonstrating that the influence of the CSEM recording system (electrodes, cables, connectors and recording device) on the repeatability of time-lapse electric field measurements is small.

5.2. Influence of near surface

To assess the influence of the heterogeneity of the near surface on the CSEM survey repeatability, we have performed a test where the CSEM signal is recorded simultaneously at the same site (site 18) with two different recording devices. For that purpose, the orientation of the two orthogonal 100m-long electric dipoles of the first station have rotated by 45° compared to the second station in order to sample different near surface terrain. The amplitudes and phases of the PE major axis of the horizontal electric field as a function of the CSEM fundamental frequencies and associated first fifth odd harmonics are shown on figure 8. It is clear that measurements agreed with each other within a few percent. We have therefore also displayed the relative variation or repeatability R (equation 7) of the amplitudes of the major PE axis between the N0 and N45 stations. For the phases, we simply calculated phase differences. Within the 1 and 100Hz band, the electric field measurements agreed within 1% (except at 50Hz due to the presence of cultural noise). Above 100Hz, electric field measurements deviate up to about 5%, possibly caused by increased levels of external noise (50 Hz harmonics and other types of cultural noise generated by the nearby industrial activities). Similarly below 1 Hz, the repeatability is poorer (3-4%) most likely caused by an increased level of external noise, here of magnetotelluric origin as evidenced by the low signal to noise ratio of the lowest frequency (1/32s). Similar conclusions hold for the phase of the electric field with less than 1° repeatability between 1 and 100Hz and 2-3 ° below 1Hz and abode 100 Hz. We therefore conclude that the heterogeneity of the near surface has a limited influence on the survey repeatability and definitely much less than external noise.

5.3. Influence of external noise

To assess the influence of external noise on the CSEM survey repeatability, we have installed station 18 twice three days apart, while the CSEM transmitter was kept unchanged. The amplitude and phase of the PE major axis of the horizontal electric field as well as their repeatability is shown on figure 9. Between 0.1Hz and 10Hz, repeatability is within 2-3%, occasionally less than 1%, and 2-3°, occasionally less than 1°, for the amplitudes and phases, respectively. At higher frequencies (>10Hz), the presence of external noise (e.g. 50Hz and harmonics) degrades the repeatability (5-10%and 5-10° for the amplitudes and phases, respectively). Similarly, at low frequencies (<0.1 Hz), the presence of low frequency MT signals degrades the repeatability (>10% and > 10° for the amplitudes and phases, respectively). These observations highlight again the prime influence of external EM noise on CSEM survey repeatability.

5.4. Overall time-lapse CSEM survey repeatability

To assess whether the aforementioned influence of external noise on survey repeatability holds for longer periods of time and between time-lapse surveys, we have compared the amplitude and phase variations of the PE major axis of the horizontal electric field at station 18 between the baseline and monitor surveys (figure 10). Over the whole frequency band, repeatability is within 2-3% and 2-3° for the amplitudes and phases, respectively but the presence of strong external noise on the baseline or monitor surveys on some specific

frequency bands (e.g. 1/32s at low frequencies, 50Hz and harmonics at high frequencies) degrades again significantly the repeatability up to 10% and 10° on the amplitudes and phases, respectively. Although weather was humid during the baseline and dry during the monitor survey, the change of the top soil water saturation and hence resistivity seems to have a limited influence on survey repeatability.

Interestingly, similar conclusions hold for the entire time-lapse dataset. Indeed, when comparing the repeatability of the amplitudes of the PE major axis of the horizontal electric field with the baseline and monitor signal to noise ratio (figure 11), the trend is a clear decrease of the repeatability R with increasing signal to noise ratio i.e. with decreasing level of external noise. Since the frequencies of interest for deep reservoir monitoring are low, we have limited our analysis to frequencies less than 10Hz. This observation demonstrates that for our time-lapse CSEM procedure, the signal to external noise ratio of the repeated EM measurements is the most important parameter to control in order to achieve a good survey repeatability. Contrary to MT monitoring experiments where the practitioner has limited control on the source strength and hence on the achievable survey repeatability, the CSEM signal to noise ratio can be controlled and increased at will by simply increasing the transmitter dipolar moment (e.g. longer electric dipole transmitter and/or stronger power generator) and/or recording signals for longer periods of time to increase the chance of stacking-out random external noise.

6. Reykjanes spatial and time-lapse CSEM results

In this section, we have first performed an inversion CSEM and MT data to confront and validate the CSEM and MT results with the logged resistivities in the RN-15/IDDP-2 well. For this calibration, we only inverted stations along a profile running from the transmitter and crossing the producing geothermal reservoir (figure 1). For the inversion, we used the 2.5D MARE2DEM inversion code (Key (2016)). We subsequently attempted to identify a time-lapse CSEM signal by analyzing CSEM amplitude and phase changes of the electric field between the baseline and monitor surveys.

6.1. 2.5D CSEM and MT inversions

6.1.1. CSEM inversion

We inverted the amplitudes of the PE major axis of the horizontal electric field from seven CSEM stations located in the vicinity of the selected profile (stations 05, 09, 14, 18, 22 and 24). Inverted frequencies were 1/32s, 1/8s, 1/2s, 2Hz, 8Hz, 32Hz and associated first firth odd harmonics up to 50Hz. Both POL1 and POL2 transmitter polarizations were inverted. Data from either the baseline or monitor survey were used depending on their signal to noise ratio. We limited the frequency band on the high side to 50 Hz due to the presence of strong external noise (e.g. 50Hz and harmonics, industrial noise). The starting model of the CSEM inversion was a homogeneous 2 Ω.m half-space. Numerical simulations of the impact of the land/ocean interface showed that stations nearby the coast may be affected by the presence of the conductive sea over a large frequency band but since the area of interest (RN-15/IDDP-2 well) is located far away from the coast (at least 2km), we did

not include it. Future 3D inversions will however require to include such an interface and will be the scope of a subsequent paper.

To assess the convergence of the inversion and quality of the data fit, we calculated RMS misfits based on measurement errors (Key (2016)). Measurement errors have been estimated from the external noise levels calculated at the processing stage. The target misfit is set to 1 and we consider the data fit to be satisfactory when misfits are small (as close as possible to unity) and have been significantly reduced during the inversion process (typically several units). Here, initial misfits were in the 10-20 range and dropped into the 2-5 range after 15 iterations, leading a satisfactory data fit over the whole frequency band (figure 12). Only station 14 has a RMS misfit great than 10, most likely due to a remaining static effect as evidenced by the similar shapes of the modelled and observed amplitude curves. To compensate for that, a second-stage static shift correction would be necessary and the inversion re-run but since misfits are already small for most of the stations, we did not perform this additional step.

The resulting resistivity model as well as the average resistivities logged in the RN-15/IDDP-2 well are displayed on the top of figure 13. The shallow conductive smectite-rich caprock is well imaged in the vicinity of the RN-15/IDDP-2 well, with a resistivity (<5 Ωm) and thickness (approximately 1200m) in good agreement with the logged values. The underlying more resistive chlorite/epidote rich layer is also imaged but deeper than 2km, the recovered resistivities are too low (20 Ωm vs 50/100 Ωm in the well). To explain this discrepancy, we have computed the Jacobian or sensitivity matrix at the last iteration of the inversion (figure 14). Higher values indicate areas where the dataset is highly sensitive to a change in resistivity. The sensitivity of the CSEM setup is clearly non-uniform with the highest sensitivity towards the mid-point between the CSEM transmitter and receiver grid (around 3km from the transmitter) i.e. in the vicinity of the RN15/IDDP-2 well (located at 3.7km distance from the transmitter), confirming that the transmitter and receiver layout is adequate for imaging resistivity variations in this area. It however also shows that the sensitivity at 4/5 km depth is low (at least two orders of magnitudes less than in the first 1.5km), possibly explaining why the resistivity values recovered from the CSEM inversion are too low compared to the logged ones. Finally, figure 14 also shows that the CSEM sensitivity is poor underneath the transmitter and the most distant receivers (distances greater than 5km from the transmitter). These low sensitivity areas explain most likely the unexpected absence of the conductive layer at large distances from the transmitter (greater than RX18) and its unexpected thickening at negative distances from the transmitter. Similarly, at shallow depth ($<$ 1.5km) between the transmitter and first receiver (RX05), artefacts may be present due to the low sensitivity of the CSEM setup. This illustrates the difficulty of imaging complex resistivity variations with only CSEM transmitter and the need for multiple transmitter positions to obtain a more homogeneous sensitivity matrix.

6.1.2. Joint CSEM and MT inversion

To compensate for the low sensitivity at depth of our CSEM setup, additional constraints (e.g. structural, petrophysical) and/or datasets (e.g. MT, resistivity logs) may be necessary (Scholl et al. (2010)). In an attempt to increase the resolution of the resistivity image at

depths greater than 2/3km, we have looked into the possibility of jointly inverting CSEM and MT over the area of interest (Abubakar et al. (2011)). Since our MT dataset is of poor quality, we used the legacy MT dataset collected over the Reykjanes geothermal field instead (Karlsdóttir and Vilhjálmsson (2016)).

We first inverted the apparent resistivities and phases of the non-diagonal components of the MT impedance tensor for seven MT stations nearby our CSEM stations along the profile of interest (figure 1). Frequencies range from 0.001Hz until 100Hz. Final RMS misfits are close to unity, providing a satisfactory data match (figure 15). The resulting resistivity model as well as the average resistivities logged in the RN-15/IDDP-2 well are displayed in the middle of figure 13. Here also, the shallow conductive smectite-rich caprock is well imaged with inverted resistivities (<5 Ωm) in good agreement with the logged values. Nevertheless, the depth of the base of this conductive layer does not match well with the well observations (a few hundreds of meters difference). Contrary to the CSEM inversion, the underlying more resistive chlorite/epidote rich layer is well imaged with highly resistive layers (up to 100Ωm at 5km depth).

To take advantage of both CSEM and MT datasets, we have jointly inverted the amplitudes of the electric field for the CSEM stations 05, 09, 14, 18, 22 and 24 with the apparent resistivities and phases of the non-diagonal components of the MT impedance tensor for MT stations 77, 76, 74, 78, 79, 70 and 139. CSEM and MT data fit are displayed on figure 12 and figure 15. Overall, misfits are small and similar to the CSEM only and MT only cases, providing a satisfactory data fit. However, RMS misfits are slightly larger than the standalone cases, simply due to the fact that additional constraints have been introduced in the inversion process by the addition of new data. The resulting resistivity model as well as the average resistivities logged in the RN15/IDDP2 well are displayed at the bottom of figure 13. Interestingly, both the shallow conductive smectite-rich caprock and the underlying resistive chlorite/epidote rich layer layer are now well imaged and in good agreement with the logged values. Furthermore, the depth of transition zone between the caprock and the deeper and more resistive material fits now very well with the well observations. This good match demonstrates the validity of CSEM and MT measurements for estimating and hence monitoring resistivity variations within the Reykjanes geothermal reservoir.

6.2. Time-lapse CSEM signals

In order to identify time-lapse signals in our dataset related to the thermal stimulation of the RN-15/IDDP2 well, we have calculated the amplitude and phase change of the polarization ellipse of the horizontal electric field between the monitor and baseline surveys (figure 16, phase not shown). We focused on the stations located along the aforementioned profile as it crosses the producing reservoir and the RN-15/IDDP-2 well. For the stations with a high signal to noise ratio and therefore high repeatability (stations 09, 14, 18, 19), no clear and consistent time-lapse anomaly related to the RN-15/IDDP-2 thermal stimulation can be identified. Indeed, observed time-lapse anomalies are random and stay within the measurement error. The only significant anomalies occur at frequencies where the signal to noise and hence repeatability is poor (e.g. 0.03125Hz, 50Hz) and are likely to be related to external sources of noise.

7. Results and Discussion

7.1. Time-lapse CSEM signals related to the RN-15/IDDP-2 thermal stimulation

Despite the high degree repeatability of the CSEM measurements between the Reykjanes baseline and monitor (a few percent on the amplitude of the electrid field), no clear and consistent time-lapse anomaly related to the RN-15/IDDP-2 thermal stimulation has been identified. A most likely explanation is related to the weakness of the time-lapse CSEM signals in comparison to the achieved repeatability. To demonstrate this, we have calculated the detectability of time-lapse CSEM signals based on electric field amplitudes as a function of the size of the stimulated zone (here, width) and measurements errors for the 2.5D Reykjanes conceptual model (figure 17). It clearly shows that the amplitude of the time-lapse signal is strongly related to the volume of the stimulated area (here, its width as its height is kept fixed at 1km). For the repeatability achieved during the actual Reykjanes time-lapse survey (a few percent), it indicates that a time-lapse signal can be observed (D greater than 1) only if the stimulated area is larger than 500m in width. During the drilling of RN-15/IDDP-2 well, high-permeability circulation-fluid loss zones were detected below 3 km depth to bottom. The largest one occurred at around 3.4 km depth with permeable zones encountered below 3.4 km accepting less than 5%percent of the injected water. It is therefore likely that most of the fluid injected during the thermal stimulation leaked into this zone between 3 and 3.4km depth. Since the total volume of injected cold water was roughly $100000m^3$ in one month and the porosity of the in-situ rock is low (a few percent), the lateral extent of the stimulated zone does not exceed a couple of hundreds meters and most likely well below the detectability threshold achieved for our actual survey. To pick such a small signal up, even more repeatable measurements would be required (less than a percent, figure 17) or alternatively, a more sensitive CSEM layout would need to be deployed (e.g. a borehole to surface CSEM configuration, Tietze et al. (2015)). Our CSEM time-lapse analysis is based on the amplitude and phase of the electric phase measurements but it is possible that other parameters are actually more sensitive to resistivity changes than the raw electric field measurements, like the distortion (Rees et al. (2016c)) or phase tensor (Booker (2014)). The computation of such parameters have however to be adapted to the CSEM case and will be the scope of a subsequent paper.

7.2. CSEM and MT imaging and monitoring of high-enthalpy geothermal reservoir

The resistivity structure of the Reykjanes geothermal field (conductive caprock overlying a more resistive high temperature reservoir) is very generic for any high-enthalpy geothermal reservoirs (Flóvenz et al. (1985), Kristinsdóttir et al. (2010), Khodayar et al. (2016)) and conclusions drawn on this particular example are therefore applicable to many other geothermal fields.

The CSEM calibration survey performed here shows such data provides reliable data for the imaging and monitoring of high-enthalpy geothermal reservoir. The main benefit relies on the high signal to noise ratios that can be achieved despite the presence of high levels of cultural noise. At this stage, the main drawback is caused by the limited depth of penetration (2-3km depth), most likely caused by the combination of a thick conductive

and hence attenuating caprock, and the limited dipolar moment of the transmitter. Greater depths of penetration can surely be achieved using more powerful transmitters (e.g. longer dipole, higher currents) as recently developed for offshore CSEM systems (Hanssen et al. (2017)). In addition, the resistivity of the overburden has to be taken into account as more resistive overburdens can often lead to greater depths of penetration (3-4km) with similar CSEM systems (Coppo et al. (2016)).

As shown on the Reykjanes example, MT data provides a good alternative to increase the depth of investigation ($>$ 2-3km) when CSEM data is of limited use. For monitoring purposes, the challenge is however to obtain a highly repeatable MT dataset (Abdelfettah et al. (2018)). Continuous MT and CSEM monitoring surely provides a good way to control the quality of the measurements by correlating them with subsurface phenomena but it also represents a huge logistical challenge for long term monitoring. Indeed, numerical simulations (figure 17, Orange et al. (2009), Wirianto et al. (2010), Thiel (2017)) show that only resistivity changes happening over a significant reservoir volume (e.g. after long periods of fluid injection/production) may lead to detectable EM signals. Time-lapse MT measurements alleviate this logistical constraint but as shown with our particular example, significant efforts have to be made to ensure sufficient data quality during both baseline and monitor MT surveys, especially when performed in highly industrialized areas with high levels of electromagnetic noise.

8. Conclusions

Monitoring resistivity changes associated to fluid movement in deep high-enthalpy geothermal reservoirs from the surface generally requires measuring small variations in EM fields and therefore high survey repeatability. This poses a real challenge in highly industrialized areas like geothermal plants, as it usually generates spatially variable and broad frequency band EM noise that can obfuscate the EM signals of interest and alter the survey repeatability, especially when using natural MT signals. Controlled-Source EM surveying may be an attractive option as the use of an transmitter allows to control and hence influence the signal repeatability.

We have investigated the benefits and drawback of such an option in actual field conditions by acquiring a time-lapse CSEM survey over the Reykjanes geothermal field. Careful survey planning and execution allows to reduce the large number of parameters influencing survey repeatability to the level of external noise of the baseline and monitor surveys. As it can be artificially influenced, it offers the possibility to adapt the survey design to increase the chance of detecting the time-lapse signals of interest. On the contrary, little control is possible on the MT signal to noise ratio and hence repeatability. The time-lapse EM survey acquired over the Reykjanes geothermal reservoir provides the basic information for deciding when and how an EM monitor survey must be performed for the monitoring of the Reykjanes reservoir but also for the definition of the monitoring strategy of similar high-enthalpy geothermal reservoirs.

Monitoring high-enthalpy geothermal reservoir development with CSEM and/or MT techniques is still at its infancy but we believe that by careful survey design and by applying

dedicated data acquisition, processing and imaging techniques, sufficient data repeatability can be achieved to monitor resistivity changes associated to fluid movements in the deep geothermal reservoirs.

Acknowledgments

The IDDP-2 was funded by HS Orka, Landsvirkjun, Orkuveita Reykjavíkur, and the National Energy Authority in Iceland, together with Statoil, the Norwegian oil and gas company. The IDDP-2 has also received funding from the DEEPEGS project, European Union's HORIZON 2020 research and innovation program under grant agreement No 690771. We would like to thank HS-ORKA for providing access to the MT dataset over the Reykjanes geothermal field. We are also very grateful to Steinthor Nielsson, Stephan Audunn Stefansson from the Iceland Geosurvey (ISOR) for their logistical support during the EM surveys. We would like also to thank Eva Schill, Nadine Haaf from the Karlsruhe Institute of Technology, Germany, Mariane Peter-Borie, Florent Beaubois and Esteban Pineda for their unvaluable help during the field work.

References

Abdelfettah, Y., Sailhac, P., Larnier, H., Matthey, P.D., Schill, E., 2018. Continuous and time-lapse magnetotelluric monitoring of low volume injection at rittershoffen geothermal project, northern alsace–france. Geothermics 71, 1–11.

Abubakar, A., Li, M., Pan, G., Liu, J., Habashy, T., 2011. Joint mt and csem data inversion using a multiplicative cost function approach. Geophysics 76, F203–F214.

Archie, G.E., et al., 1942. The electrical resistivity log as an aid in determining some reservoir characteristics. Transactions of the AIME 146, 54–62.

Arnórsson, S., 1995. Geothermal systems in iceland: structure and conceptual models—i. high-temperature areas. Geothermics 24, 561–602.

Bibby, H., Caldwell, T., Brown, C., 2005. Determinable and non-determinable parameters of galvanic distortion in magnetotellurics. Geophysical Journal International 163, 915–930.

Björnsson, S., Arnorsson, S., Tomasson, J., 1970. Exploration of the reykianes thermal brine area. Geothermics 2, 1640–1650.

Booker, J.R., 2014. The magnetotelluric phase tensor: a critical review. Surveys in Geophysics 35, 7–40.

Börner, J.H., Herdegen, V., Repke, J.U., Spitzer, K., 2015a. The electrical conductivity of co2-bearing pore waters at elevated pressure and temperature: a laboratory study and its implications in co2 storage monitoring and leakage detection. Geophysical Journal International 203, 1072–1084.

Börner, J.H., Wang, F., Weißflog, J., Bär, M., Görz, I., Spitzer, K., 2015b. Multi-method virtual electromagnetic experiments for developing suitable monitoring designs: A fictitious co2 sequestration scenario in northern germany. Geophysical Prospecting 63, 1430–1449.

Cagniard, L., 1953. Basic theory of the magneto-telluric method of geophysical prospecting. Geophysics 18, 605–635.

Chave, A.D., Jones, A.G., 2012. The magnetotelluric method: Theory and practice. Cambridge University Press.

Chave, A.D., Thomson, D.J., 1989. Some comments on magnetotelluric response function estimation. Journal of Geophysical Research: Solid Earth 94, 14215–14225.

Chave, A.D., Thomson, D.J., 2004. Bounded influence magnetotelluric response function estimation. Geophysical Journal International 157, 988–1006.

Commer, M., Newman, G.A., 2009. Three-dimensional controlled-source electromagnetic and magnetotelluric joint inversion. Geophysical Journal International 178, 1305–1316.

Constable, S., Key, K., Lewis, L., 2009. Mapping offshore sedimentary structure using electromagnetic methods and terrain effects in marine magnetotelluric data. Geophysical Journal International 176, 431–442.

Constable, S., Weiss, C.J., 2006. Mapping thin resistors and hydrocarbons with marine em methods: Insights from 1d modeling. Geophysics 71, G43–G51.

Coppo, N., Darnet, M., Harcouet-Menou, V., Wawrzyniak, P., Manzella, A., Bretaudeau, F., Romano, G., Lagrou, D., Girard, J.F., 2016. Characterization of deep geothermal energy resources in low enthalpy sedimentary basins in belgium using electro-magnetic methods–csem and mt results, in: European Geothermal Congress 2016.

Didana, Y.L., Heinson, G., Thiel, S., Krieger, L., 2017. Magnetotelluric monitoring of permeability enhancement at enhanced geothermal system project. Geothermics 66, 23–38.

Flóvenz, Ó.G., Georgsson, L.S., Árnason, K., 1985. Resistivity structure of the upper crust in iceland. Journal of Geophysical Research: Solid Earth 90, 10136–10150.

Frileifsson, G.Ó., Elders, W.A., Zierenberg, R.A., Stefánsson, A., Fowler, A.P., Weisenberger, T.B., Hararson, B.S., Mesfin, K.G., 2017. The iceland deep drilling project 4.5 km deep well, iddp-2, in the seawater-recharged reykjanes geothermal field in sw iceland has successfully reached its supercritical target. Scientific Drilling 23, 1.

Goubau, W.M., Gamble, T.D., Clarke, J., 1978. Magnetotelluric data analysis: removal of bias. Geophysics 43, 1157–1166.

Grayver, A.V., Streich, R., Ritter, O., 2014. 3d inversion and resolution analysis of land-based csem data from the ketzin co 2 storage formation. Geophysics 79, E101–E114.

Gudmundsdottir, V., 2015. Svartsengi – reykjanes: Reservoir temperature and pressure monitoring report 2014. Iceland GeoSurvey report ISOR-2015/026.

Gudnason, E. A., A.K.G.K., Flovenz, O.G., 2015. Seismic activity on reykjanes december 2014 – november 2015. Iceland GeoSurvey report ISOR-2015/068.

Hanssen, P., Nguyen, A.K., Fogelin, L.T., Jensen, H.R., Skarø, M., Mittet, R., Rosenquist, M., Súilleabháin, L.Ó., van der Sman, P., 2017. The next generation offshore csem acquisition system , 1194–1198.

Karlsdottir, R., Vilhjalmsson, A.M., 2014. Reykjanes geothermal area, southwest iceland. extension of 3d inversion of mt data. Iceland GeoSurvey report ISOR-2014/016.

Karlsdóttir, R., Vilhjálmsson, A.M., 2016. Sandvík, reykjanes peninsula. 3d inversion of mt data. H2020 DEEPEGS report ÍSOR-2016/041.

Key, K., 2016. Mare2dem: a 2-d inversion code for controlled-source electromagnetic and magnetotelluric data. Geophysical Journal International 207, 571–588.

Key, K., Ovall, J., 2011. A parallel goal-oriented adaptive finite element method for 2.5-d electromagnetic modelling. Geophysical Journal International 186, 137–154.

Khodayar, M., Nielsson, S., Hickson C., Gudnason, E., Hardarson, B., Gudmundsdottir, V., Halldorsdottir, S., Oskarsson, F., Weisenberger, T., Bjornsson, S., 2016. The 2016 conceptual model of reykjanes geothermal system, sw iceland. DEEPEGS Report ÍSOR-2016/072.

Kristinsdóttir, L.H., Flóvenz, Ó.G., Árnason, K., Bruhn, D., Milsch, H., Spangenberg, E., Kulenkampff, J., 2010. Electrical conductivity and p-wave velocity in rock samples from high-temperature icelandic geothermal fields. Geothermics 39, 94–105.

Kummerow, J., Raab, S., 2015. Temperature dependence of electrical resistivity-part i: Experimental investigations of hydrothermal fluids. Energy Procedia 76, 240–246.

Leroy, P., Revil, A., 2004. A triple-layer model of the surface electrochemical properties of clay minerals. Journal of Colloid and Interface Science 270, 371–380.

Munoz, G., 2014. Exploring for geothermal resources with electromagnetic methods. Surveys in geophysics 35, 101–122.

Nono, F., Gibert, B., Parat, F., Loggia, D., Cichy, S.B., Violay, M., 2018. Electrical conductivity of icelandic deep geothermal reservoirs up to supercritical conditions: Insight from laboratory experiments. Journal of Volcanology and Geothermal Research .

Ogaya, X., Ledo, J., Queralt, P., Jones, A.G., Marcuello, Á., 2016. A layer stripping approach for monitoring

resistivity variations using surface magnetotelluric responses. Journal of Applied Geophysics 132, 100–115.
Orange, A., Key, K., Constable, S., 2009. The feasibility of reservoir monitoring using time-lapse marine csem. Geophysics 74, F21–F29.
Óskarsson, F., Fridriksson, T., Thorbjörnsson, D., 2015. Geochemical monitoring of the reykjanes geothermal reservoir 2003 to 2013, in: Proc. World Geothermal Congress.
Peacock, J.R., Thiel, S., Heinson, G.S., Reid, P., 2013. Time-lapse magnetotelluric monitoring of an enhanced geothermal system. Geophysics 78, B121–B130.
Rees, N., Carter, S., Heinson, G., Krieger, L., 2016a. Monitoring shale gas resources in the cooper basin using magnetotellurics. Geophysics 81, A13–A16.
Rees, N., Carter, S., Heinson, G., Krieger, L., Conway, D., Boren, G., Matthews, C., 2016b. Magnetotelluric monitoring of coal-seam gas and shale-gas resource development in australia. The Leading Edge 35, 64–70.
Rees, N., Heinson, G., Krieger, L., 2016c. Magnetotelluric monitoring of coal seam gas depressurization. Geophysics 81, E423–E432.
Reinsch, T., 2016. Physical properties of rock at reservoir conditions. FP7 IMAGE Report .
Reinsch, T., Dobson, P., Asanuma, H., Huenges, E., Poletto, F., Sanjuan, B., 2017. Utilizing supercritical geothermal systems: a review of past ventures and ongoing research activities. Geothermal Energy 5, 16.
Scholl, C., Hallinan, S., Miorelli, F., Watts, M., 2010. Geological consistency from inversions of geophysical data. 79th EAGE Conference and Exhibition 2017 .
Sims, W., Bostick Jr, F., Smith, H., 1971. The estimation of magnetotelluric impedance tensor elements from measured data. Geophysics 36, 938–942.
Siripunvaraporn, W., Bedrosian, P.A., Li, Y., Patro, P.K., Spitzer, K., Toh, H., 2018. Special issue "studies on electromagnetic induction in the earth: recent advances". Earth, Planets and Space 70, 47.
Smai, F., Wawrzyniak, P., submitted. Razorback, an open source python library for robust processing of magnetotelluric data. Geophysical Prospecting .
Spichak, V., Manzella, A., 2009. Electromagnetic sounding of geothermal zones. Journal of Applied Geophysics 68, 459–478.
Stefanson, A., Gislason, D., Sigurosson, Fridleifsson, G., 2017. The drilling of rn-15/iddp-2 research well at reykjanes in sw iceland. Geotherm Resour Counc Trans , 512–522.
Streich, R., 2016. Controlled-source electromagnetic approaches for hydrocarbon exploration and monitoring on land. Surveys in Geophysics 37, 47–80.
Streich, R., Becken, M., Ritter, O., 2010. Imaging of co 2 storage sites, geothermal reservoirs, and gas shales using controlled-source magnetotellurics: modeling studies. Chemie der Erde-Geochemistry 70, 63–75.
Streich, R., Becken, M., Ritter, O., 2013. Robust processing of noisy land-based controlled-source electromagnetic data. Geophysics 78, E237–E247.
Thiel, S., 2017. Electromagnetic monitoring of hydraulic fracturing: Relationship to permeability, seismicity, and stress. Surveys in Geophysics , 1–37.
Tietze, K., Ritter, O., Veeken, P., 2015. Controlled-source electromagnetic monitoring of reservoir oil saturation using a novel borehole-to-surface configuration. Geophysical Prospecting 63, 1468–1490.
Tómasson, J., Kristmannsdóttir, H., 1972. High temperature alteration minerals and thermal brines, reykjanes, iceland. Contributions to Mineralogy and Petrology 36, 123–134.
Vozoff, K., 1972. The magnetotelluric method in the exploration of sedimentary basins. Geophysics 37, 98–141.
Weidelt, P., 2007. Guided waves in marine csem. Geophysical Journal International 171, 153–176.
Wirianto, M., Mulder, W., Slob, E., 2010. A feasibility study of land csem reservoir monitoring in a complex 3-d model. Geophysical Journal International 181, 741–755.
Zonge, K.L., Hughes, L.J., Nabighian, M., 1991. Electromagnetic methods in applied geophysics. Society of Exploration Geophysicists, SEG Electromagnetic methods in applied geophysics.

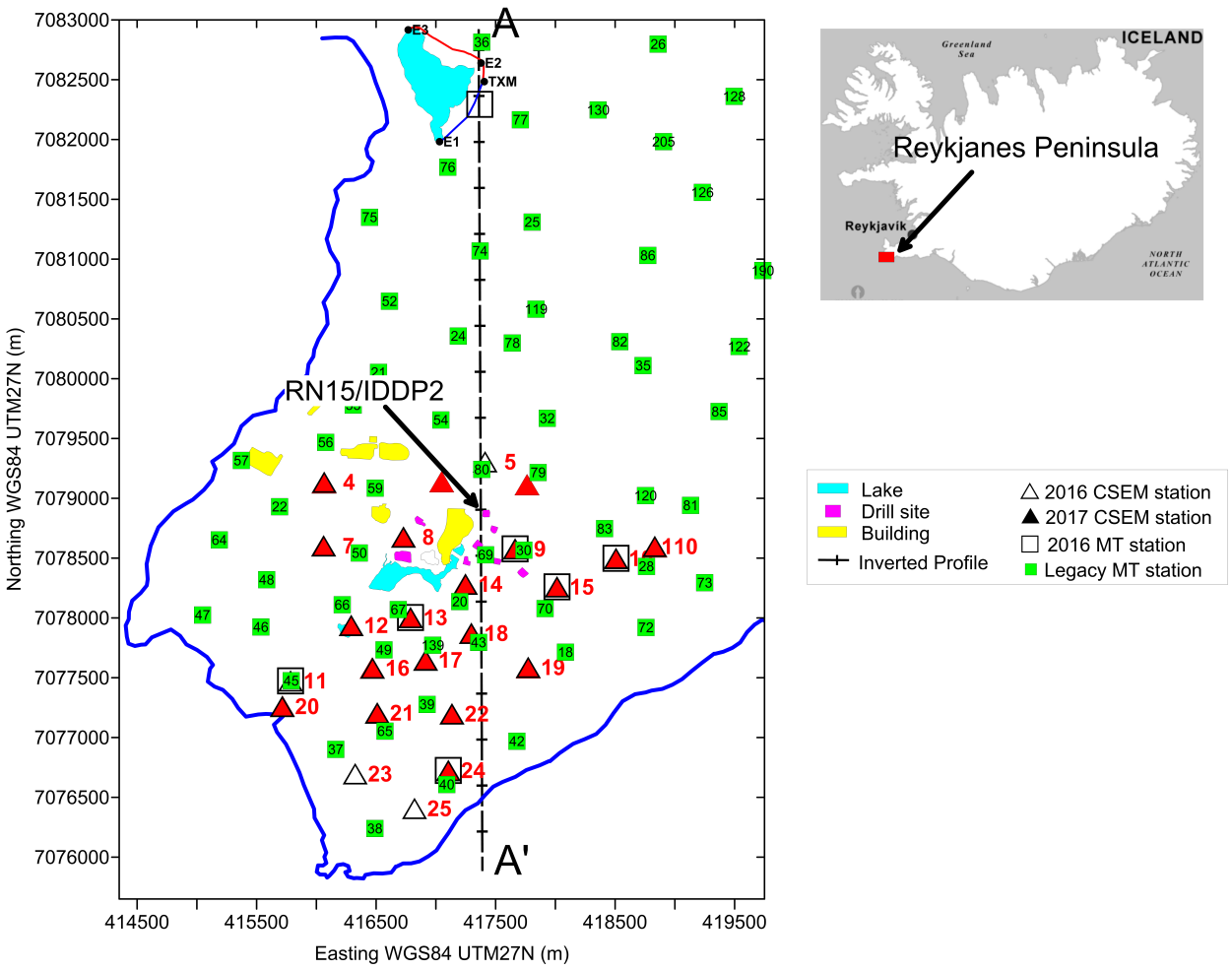

Figure 1: **Map of the Reykjanes geothermal field and time-lapse CSEM and MT survey layout. CSEM transmitter is labelled TXM and recording stations with numbers. Section AA' represents the axis of 2.5D inverted model.**

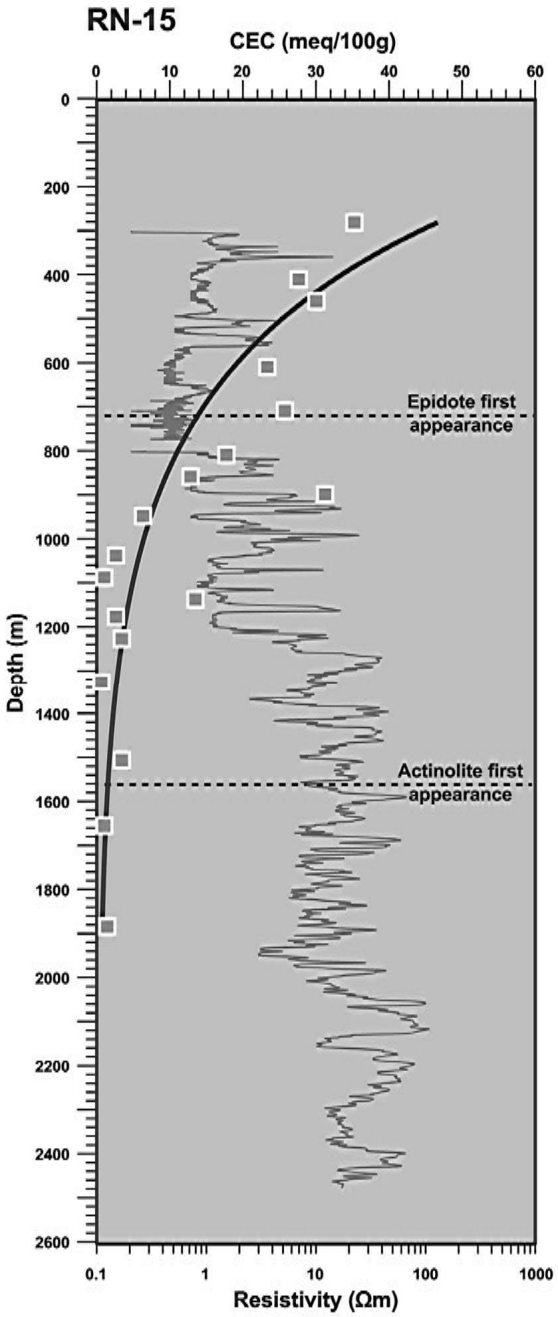

Figure 2: **Logged resistivity in the RN-15, subsequently DEEPEGS/IDDP-2 well (solid gray line) and Cation Exchange Capacity (square) measured in laboratory conditions from cuttings, a function of the depth below surface (modified from Reinsch (2016)).**

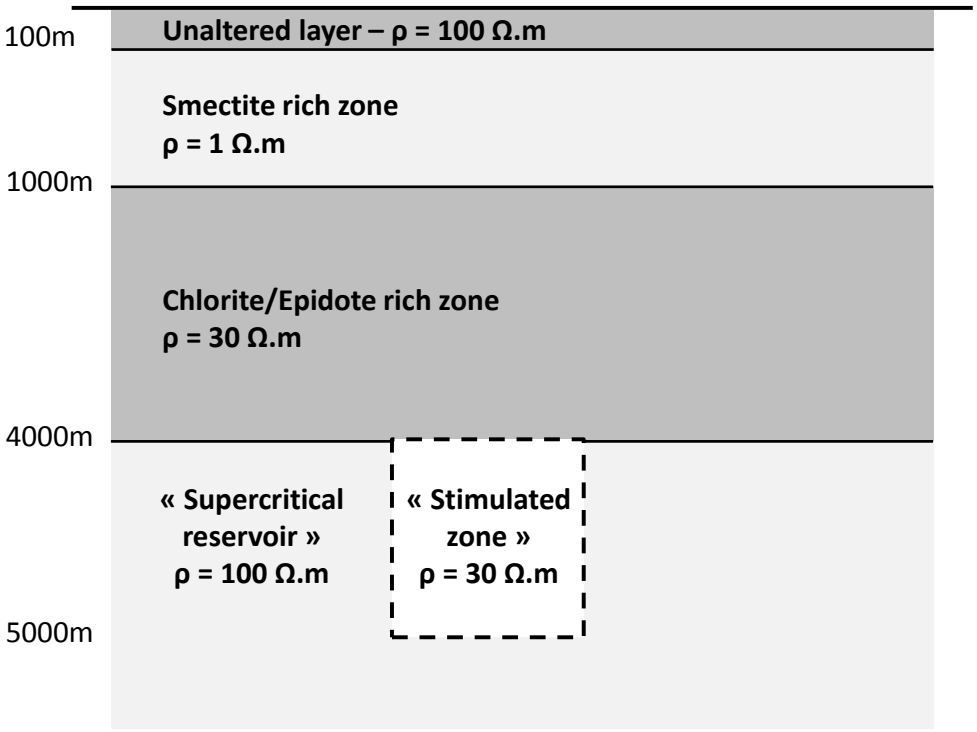

Figure 3: **Simplified resistivity model of the Reykjanes geothermal field. Depth scale is arbitrary.**

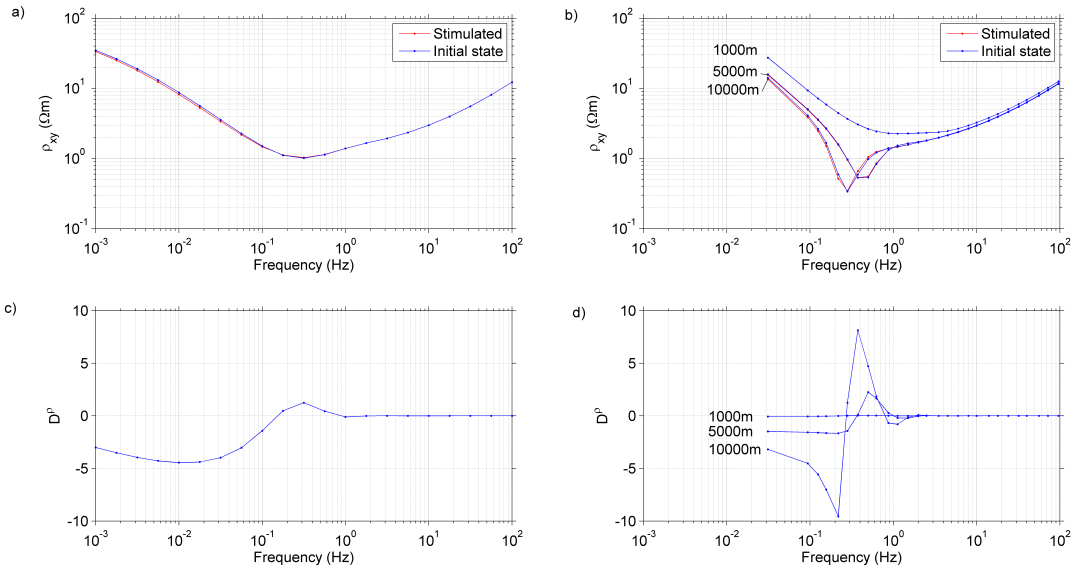

Figure 4: **a) MT and b) CSEM apparent resistivity curves for the simplified 1D resistivity model of the Reykjanes geothermal field with a 100Ωm (initial state) and 30Ωm (stimulated) 1km thick layer at 4km depth. c) MT and d) CSEM detectability of the 100Ωm to 30Ωm resistivity change over 1km at 4km depth. Offsets between the CSEM transmitter and receivers are displayed on the figure.**

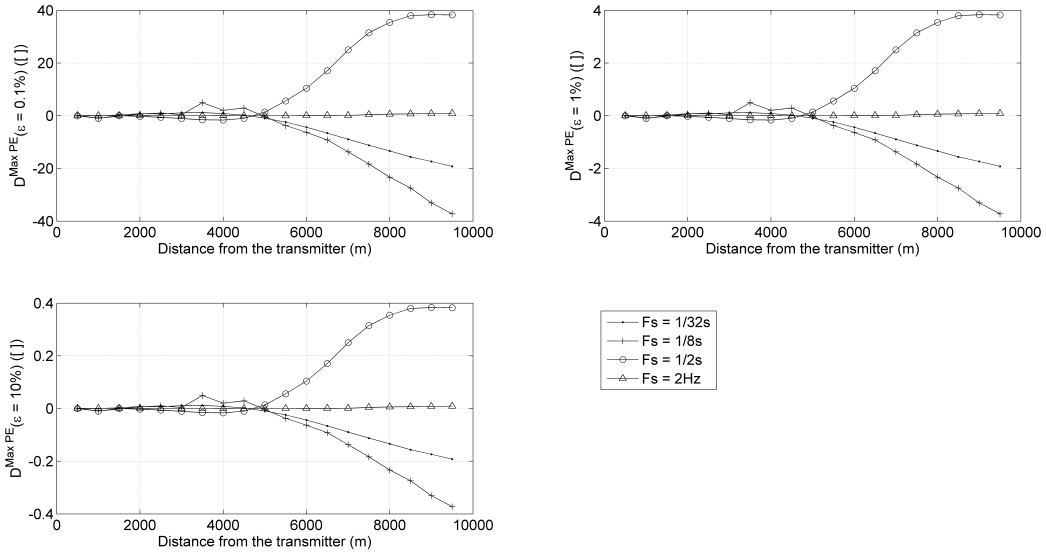

Figure 5: **Detectability of the time-lapse CSEM signal on the amplitudes of the electric field calculated on the Reykjanes 2.5D resistivity model (figure 4) as a function of the distance from the electric dipole transmitter and for different measurement errors (0.1% (top left), 1% (top right) and 10% (bottom left) of the total electric field). On each panel, each curve corresponds to a different transmitter frequency (see legend for the actual frequencies). Stimulated zone extends from 3000 to 6000m offset from the transmitter.**

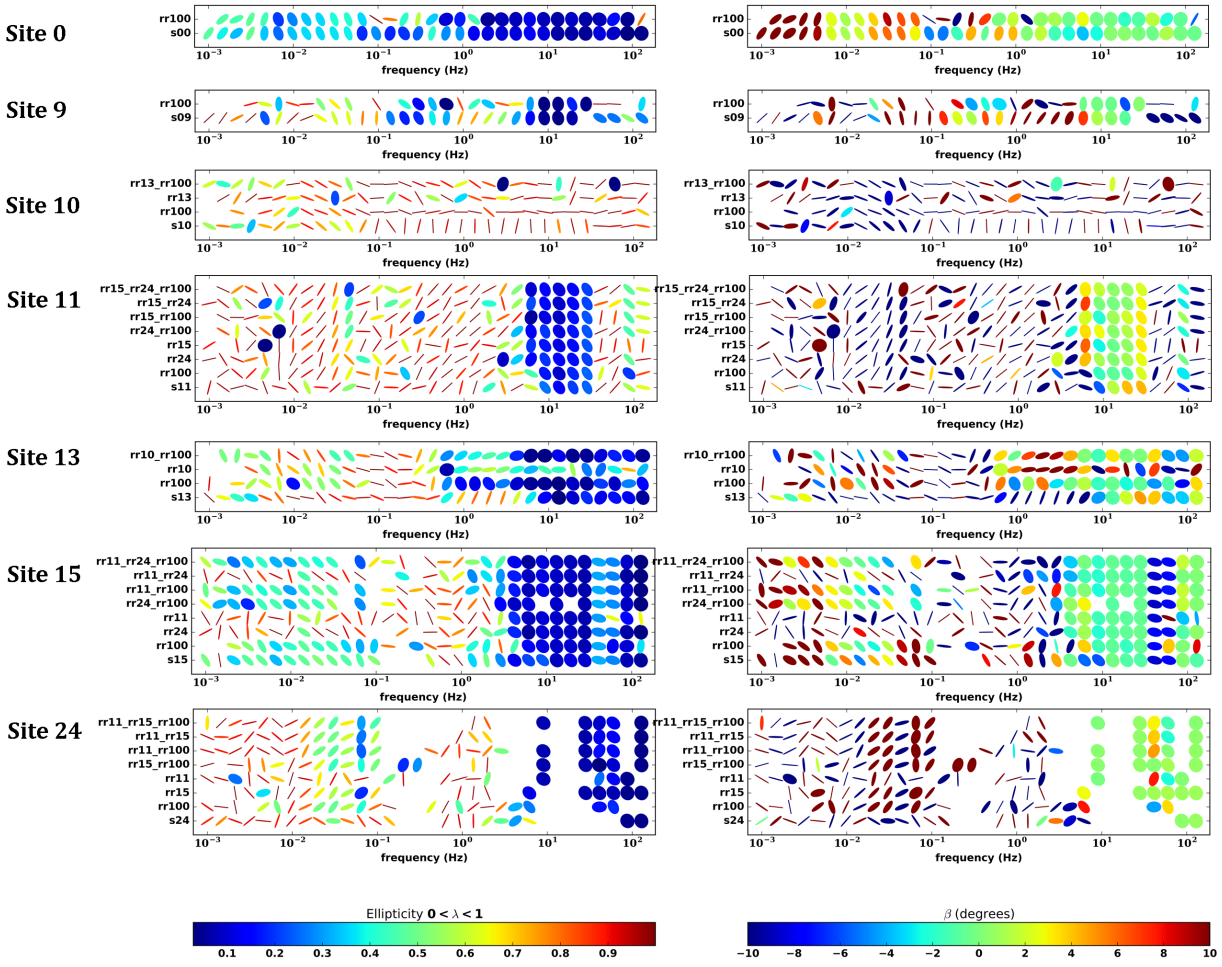

Figure 6: **Multiple remote reference two-stage bounded influence processing results. Comparison of normalized phase tensor (PT) for each possible combination of remote reference. PT are filled with color bar indexed on their ellipticity value (left panel) and their β angle value (right panel)**

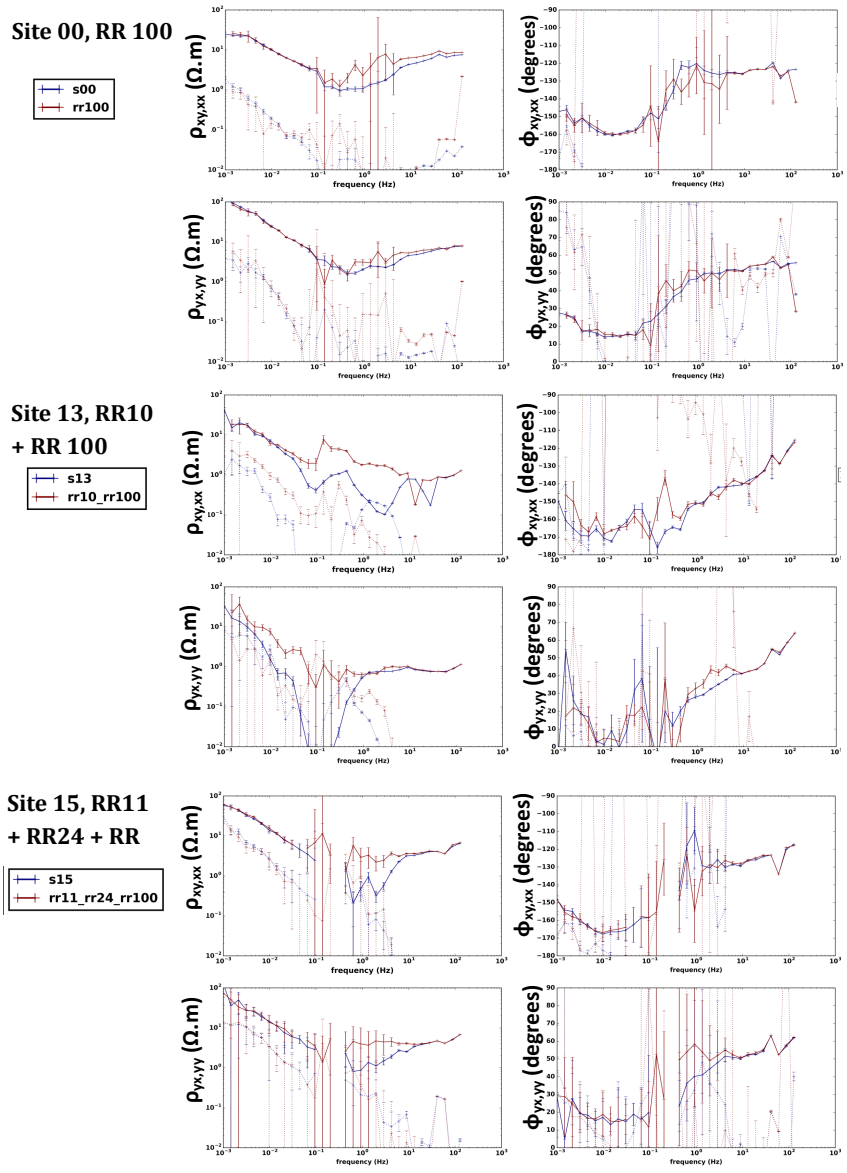

Figure 7: **MT soundings for Single Site (blue curves) and maximum number of remote reference processing for sites 00, 13 and 15 (red curves). Apparent resistivity curves ρ_{xy} and ρ_{yx} and phases ϕ_{xy} and ϕ_{yx} are shown in continuous lines, components xx and yy in dashed lines.**

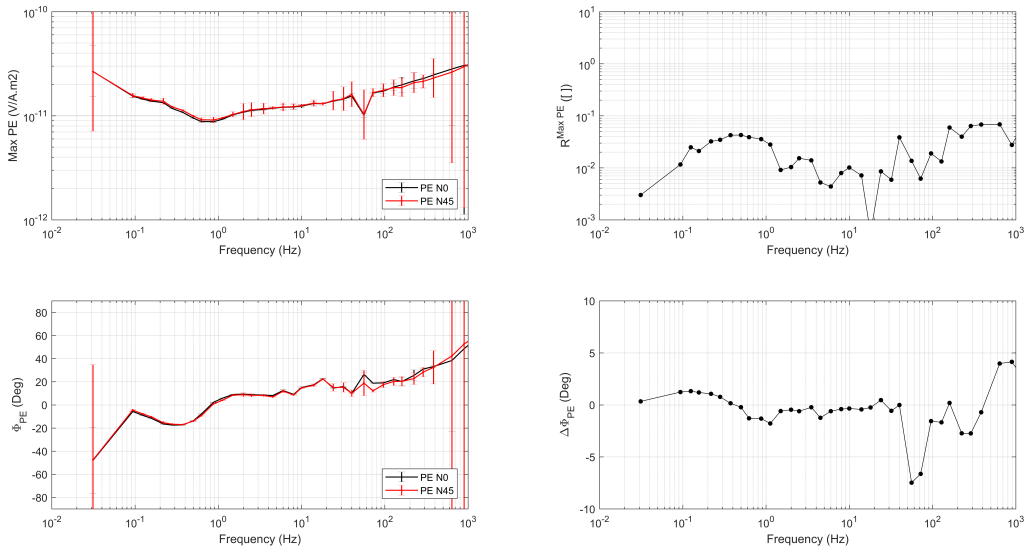

Figure 8: **Left: Amplitudes (top) and phases (bottom) of the major axis of the polarization ellipses of the horizontal electric fields measured on a N0 (black) and N45 (red) oriented station 18 measured simultaneously, as a function of the CSEM fundamental frequencies and associated first fifth odd harmonics. Noise estimates are displayed as errorbars. Right: Repeatability R of the amplitudes (top) and phase difference (bottom) of the major axis of the polarization ellipses of the horizontal electric fields between a N0 and N45 oriented station 18 measured simultaneously, as a function of the CSEM fundamental frequencies and associated first fifth odd harmonics.**

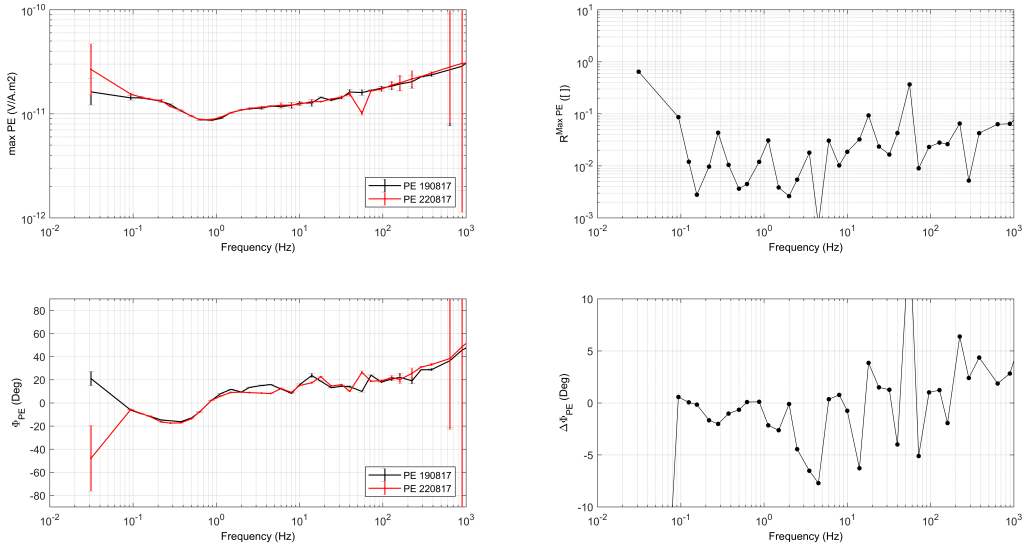

Figure 9: **Left: Amplitudes (top) and phases (bottom) of the PE major axis of the horizontal electric field measured at station 18 on Aug 19th (black) and Aug 22nd 2017 (red) as a function of the CSEM fundamental frequencies and associated first fifth odd harmonics. Noise estimates are displayed as errorbars. Right: Repeatability R of the amplitudes (top) and phase difference (bottom) of the PE major axis of the horizontal electric field between station 18 measured on Aug 19th and Aug 22nd as a function of the CSEM fundamental frequencies and associated first fifth odd harmonics.**

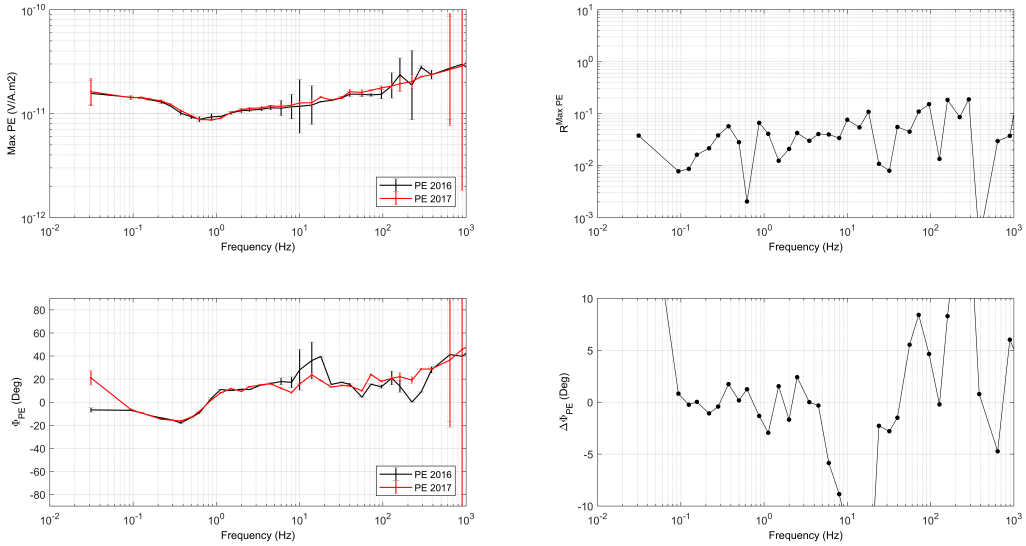

Figure 10: **Left: amplitudes (top) and phases (bottom) of the PE major axis of the horizontal electric field measured at station 18 during the baseline (black) and monitor (red) surveys as a function of the CSEM fundamental frequencies and associated first fifth odd harmonics. Noise estimates are displayed as errorbars. Right: Repeatability R of the amplitudes (top) and phase difference (bottom) of the PE major axis of the horizontal electric field between station 18 measured during baseline and monitor surveys as a function of the CSEM fundamental frequencies and associated first fifth odd harmonics.**

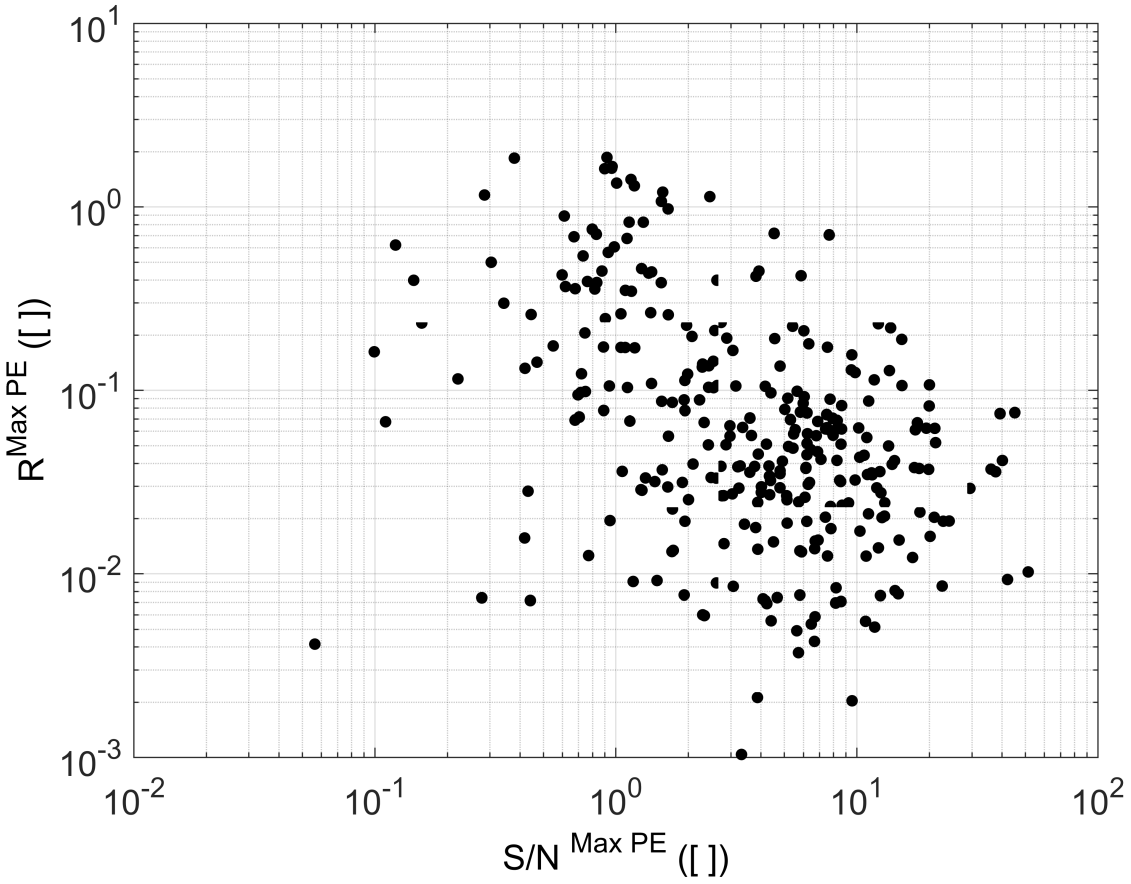

Figure 11: **Repeatability R of the amplitudes of the major PE axis of the horizontal electric fields between the baseline and monitor surveys as a function of the combined baseline and monitor signal to noise (S/N) ratios on their amplitudes. Only CSEM fundamental frequencies and associated first fifth odd harmonics less than 10Hz are displayed.**

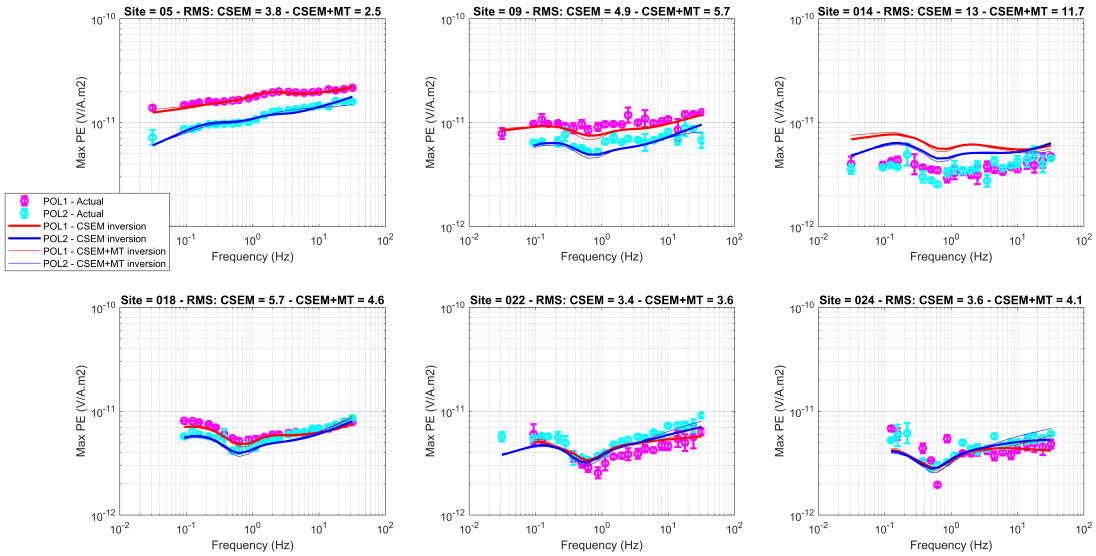

Figure 12: **Observed (dots) and modelled (solid lines) after 2.5D inversion of the amplitudes of the major axis of the polarization ellipses of the horizontal electric field as a function of the CSEM frequencies for POL1 (red/magenta) and POL2 (blue/cyan) transmitter polarizations for stations 05, 09, 14, 18, 22 and 24. Each panel corresponds to a different CSEM receiver along the inversion line. Measurement errors are displayed as vertical bars. Thin and thick solid modelled curves corresponds to the CSEM only and joint CSEM and MT inversions, respectively.**

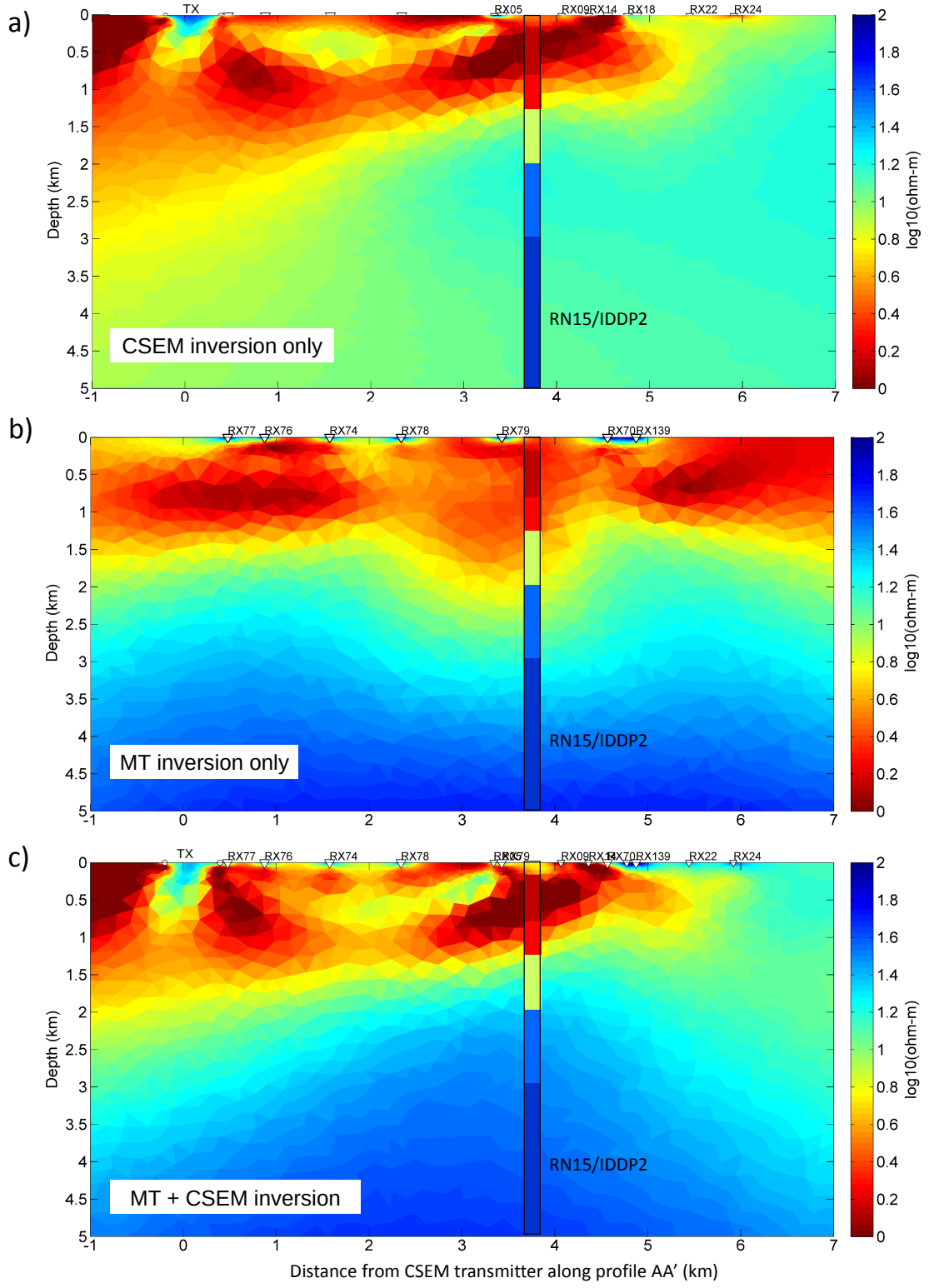

Figure 13: **a) Resistivity model (log scale) obtained after the 2.5D inversion of the CSEM data only from CSEM stations 05, 09, 14, 18, 22 and 24. b) Resistivity model (log scale) obtained after the 2.5D inversion of the MT data only from MT stations 77, 76, 74, 78, 79, 70 and 139. c) Resistivity model (log scale) obtained after the joint 2.5D inversion of CSEM data from CSEM stations 05, 09, 14, 18, 22 and 24 and MT data from MT stations 77, 76, 74, 78, 79, 70 and 139.**

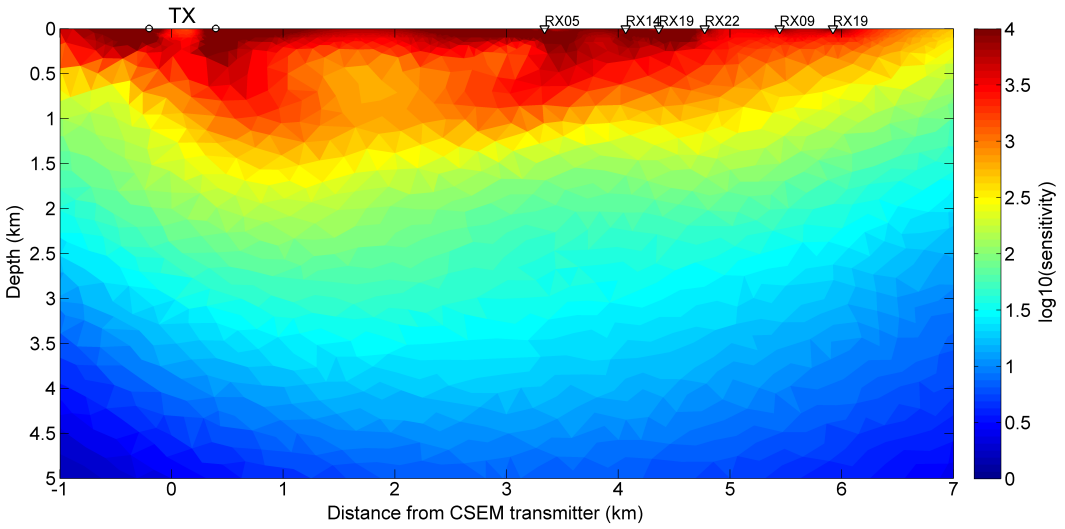

Figure 14: **Sensitivity model (Jacobian matrix in log scale) obtained after the 2.5D CSEM inversion of the stations 05, 09, 14, 18, 22 and 24.**

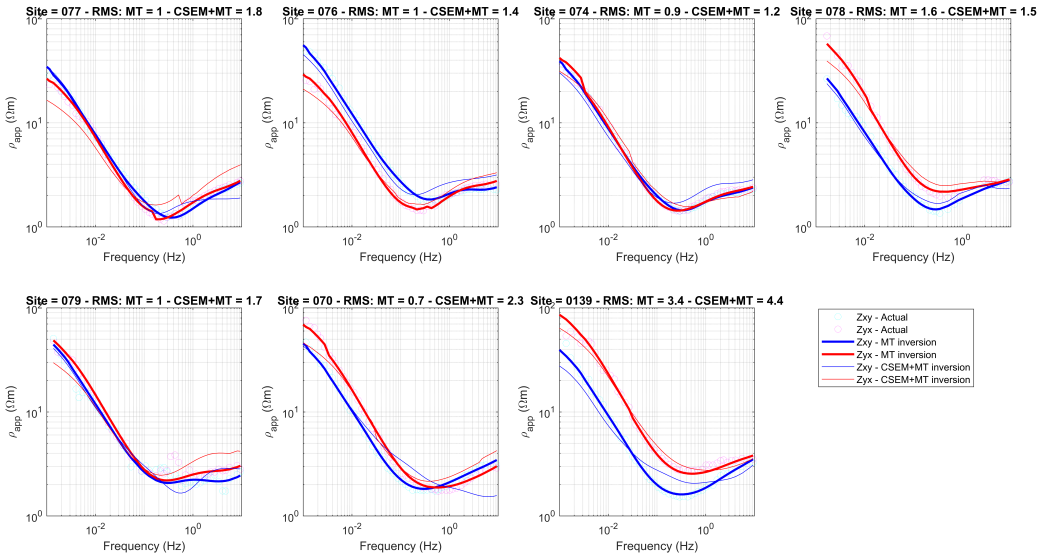

Figure 15: **Observed (dots) and modelled (solid lines) after 2.5D inversion of the amplitudes and phases of the non-diagonal components of the MT impedance tensor as a function of frequency for MT stations 77, 76, 74, 78, 79, 70 and 139. Each panel corresponds to a different MT station along the inversion line. Thin and thick solid modelled curves corresponds to the MT only and joint CSEM and MT inversions, respectively.**

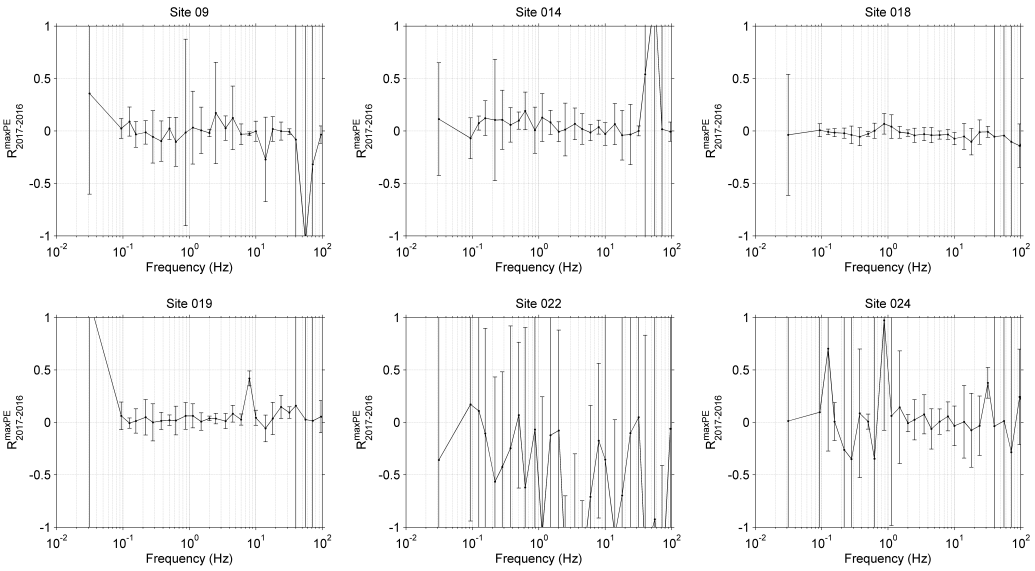

Figure 16: **Relative amplitude change of the major axis of the polarization ellipse of the horizontal electric field for the stations 09, 14, 18, 19, 22 and 24 between the monitor and baseline CSEM surveys as a function of frequency. Vertical bars indicate the estimated time-lapse amplitude measurement error.**

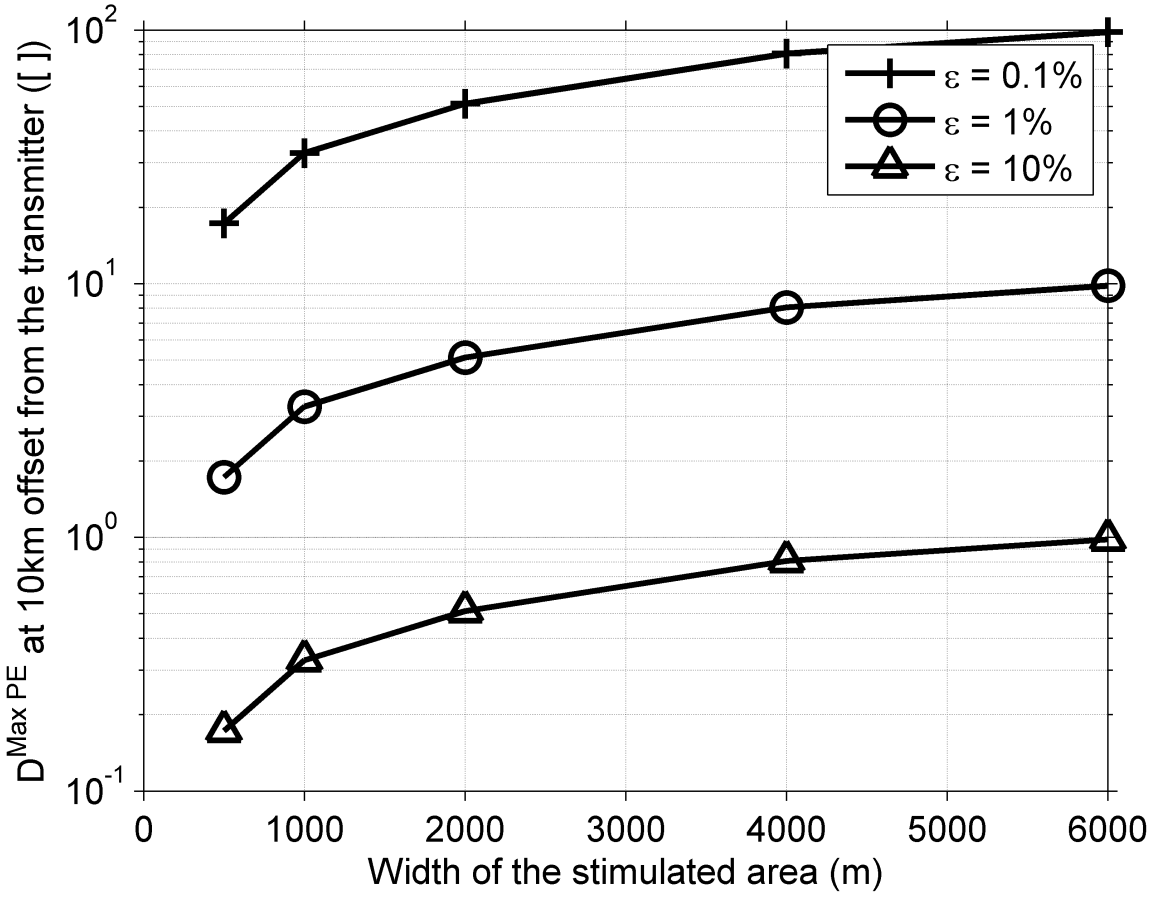

Figure 17: **Detectability of the CSEM time-lapse signal based on the amplitudes of the electric field at 10km offset from the transmitter as function of the width of the stimulated area and measurement errors for the 2.5D Reykjanes resistivity model (figure 4). Measurement errors are expressed as a percentage of the total electric field.**